

1 **Predicting Deep-Seated Landslide Displacements in Lushan Mountains through the**
2 **Integration of Convolutional Neural Networks and an Age of Exploration-Inspired Optimizer**

3 Jui-Sheng Chou^{1,*}, Hoang-Minh Nguyen¹, Huy-Phuong Phan¹, Kuo-Lung Wang²

4 ¹Department of Civil and Construction Engineering, National Taiwan University of Science and Technology, Taipei, Taiwan

5 ²Department of Civil Engineering, National Chi Nan University, Nantou, Taiwan

6 (jschou@mail.ntust.edu.tw; hoangminhkg1992@gmail.com; huyphuong777@gmail.com; klwang@ncnu.edu.tw)

7 *Correspondence e-mail address: jschou@mail.ntust.edu.tw

8 **Abstract**

9 ~~Deep-seated landslides, becoming increasingly frequent due to changing climate patterns, pose significant~~
10 ~~risks to human life and infrastructure. This research contributes to~~ landslides have caused substantial
11 damage to both human life and infrastructure in the past. Developing an early warning system for this type
12 of disaster is crucial to reduce its impact on society. This research contributes to developing predictive
13 early warning systems for deep-seated slope displacements by employing advanced computational models
14 for environmental risk management. Our novel framework integrates machine learning, time series deep
15 learning, and convolutional neural networks (CNN), enhanced by the Age of Exploration-Inspired
16 Optimizer (AEIO) algorithm. Our approach demonstrates exceptional forecasting capabilities by utilizing
17 eight years of comprehensive data—including displacement, groundwater levels, and meteorological
18 information from the Lushan Mountain region in Taiwan. The AEIO-MobileNet model ~~stands out for its~~
19 ~~precision is precise~~ in predicting imminent slope displacements with a mean absolute percentage error
20 (MAPE) of 2.81%. These advancements significantly enhance geohazard informatics by providing
21 reliable and efficient landslide risk assessment and management tools. These safeguard road networks,
22 construction projects, and infrastructure within vulnerable slope areas.

23 **Keywords:** deep-seated landslide; displacement forecasting; landslide risk assessment; early warning
24 system; machine learning; time-series deep learning; convolutional neural network; metaheuristic
25 optimization.

26 **1. Introduction**

27 ~~The 378 landslides recorded worldwide between 1997 and 2017 resulted in the deaths of 18,414~~
28 ~~people and left 4.8 million others injured, with associated costs estimated at around USD 8 billion~~
29 ~~(Ageenko et al., 2022)~~ Landslides are among the most devastating natural disasters (Huang and Fan, 2013),
30 claiming an average of over 4,000 lives annually worldwide between 2004 and 2010 (Petley, 2012).
31 Landslides represent a global hazard, particularly in developing countries, where rapid urbanization,
32 population growth, and significant land use changes occur (Caleca et al., 2024). The identification,
33 management, and monitoring of landslides are made difficult by the diversity of their types (shallow slides,

34 deep-seated slides, rock falls, rock slides, debris flows) and the complexity of their categorization based
35 on triggers, material composition, movement speed, and other characteristics (Das et al., 2022; Hungr et
36 al., 2014). These issues are further exacerbated in countries with complex geological and climatic
37 conditions.

38 ~~Deep-seated landslides, or gravitational deformations, involve slow movement of soil or rock at~~
39 ~~depths greater than 10m, impacting large areas and leading to significant debris flows (Dou et al., 2015).~~
40 A deep-seated landslide involves the gradual and persistent displacement of a substantial amount of soil
41 and rock, which can escalate into a sudden and devastating event (Kilburn and Petley, 2003; Geertsema
42 et al., 2006; Chigira, 2009). Unlike shallow landslides, which typically affect surface layers to a few
43 meters, deep-seated landslides extend deeper, often exceeding 10 meters, and can involve the movement
44 of underlying bedrock (Lin et al., 2013). Predicting these events is challenging and costly (Thai Pham et
45 al., 2019). Therefore, extensive efforts have been made to predict such disasters throughout history. One
46 method that has been employed involves thoroughly examining the physical and geological characteristics
47 of the mountainous areas at risk of landslides (Cotecchia et al., 2020). Furthermore, the level of
48 groundwater has been shown by numerous studies in the past to influence the mechanisms behind
49 landslide formation significantly (Miao and Wang, 2023; Preisig, 2020). ~~Consequently, in this study,~~
50 ~~groundwater levels will serve as inputs for models designed to predict landslides.~~

51 In pursuing a generalized approach to landslide forecasting, researchers have determined that the
52 critical factors associated with slope instability exhibit temporal variability, necessitating using time series
53 data (Chae et al., 2017). This approach combines slope deformation data collected through sensors drilled
54 deep into the slope bed with data on the natural conditions of the monitoring area, which is collected
55 simultaneously. Upon establishing that the data pertinent to landslide prediction falls within the category
56 of time series data, a formidable challenge in research related to this type of disaster is devising a predictive
57 model capable of forecasting the likelihood of such catastrophes based on related factors.

58 One of the most effective solutions for constructing models to predict time series data involves
59 applying data-driven techniques. The advancement of computational capabilities has driven the
60 widespread adoption of data-driven machine-learning models over physics-based models. This shift is
61 based on the premise that the data used for slope monitoring originates from nonlinear systems (Zhou et
62 al., 2018). ~~In contemporary times,~~ An increasing array of novel data-driven solutions is being developed
63 to overcome the constraints of traditional machine-learning approaches. ~~Among these data-driven~~
64 ~~solutions, convolutional neural networks (CNN) have emerged as one of the most effective methods.~~
65 These CNN models, which excel at automated feature extraction, can enhance efficiency in analyzing
66 complex datasets and improve the accuracy of prediction results (Alzubaidi et al., 2021).

67 Moreover, there is a noteworthy recent trend in employing metaheuristic optimization algorithms to
68 fine-tune the hyperparameters of artificial intelligence (AI) models, thereby augmenting their efficiency.
69 This approach has found application in geological and construction studies and other fields, showcasing
70 substantial effectiveness. Consequently, the fine-tuning of hyperparameters represents a potent avenue for
71 elevating the efficiency of AI models in research focused on predicting deep-seated displacements.

72 Leveraging the effective methodologies mentioned above, this study employs AI models optimized
73 by an innovative metaheuristic optimization algorithm to predict deep-seated ~~landslides displacement~~
74 the northern slope of Lushan Mountain in ~~Ren'ai~~ Ren'ai Township, Nantou County. The geological
75 characteristics of this area have undergone extensive research (Wang et al., 2015; Lin et al., 2020).
76 Previous studies have identified varying depths of the shear plane. Specifically, Lin et al. (2020)
77 determined the depth of the shear plane is 85m and 106m based on inclinometer data. This research paper
78 is firmly grounded in empirical evidence meticulously collected over eight years from extensometers at
79 depths of 70 and 40 meters. Our analysis also considers the cumulative impact of storms and heavy rainfall
80 on groundwater levels, utilizing data from four stations measuring groundwater levels in the study area
81 and other weather conditions that potentially trigger landslides. The objectives of our research were as
82 follows:

- 83 1) To analyze the application of machine learning and deep learning methods to time series data to forecast
84 short-term, deep-seated slope displacements across the Lushan Mountain area.
- 85 2) To identify the optimal model and hyperparameters for accurately forecasting deep-seated
86 displacements in the study area.
- 87 3) To evaluate the role of metaheuristic optimization algorithms in fine-tuning the hyperparameters of AI
88 models.

89 This study represents the first instance of AI models being utilized to predict deep-seated landslides
90 in Lushan Mountain. Additionally, it marks the inaugural application of AEIO for fine-tuning AI models
91 in landslide-related research. Our findings provide a valuable resource for civil engineers, contractors, and
92 inspectors involved in the planning and monitoring of construction projects in landslide-prone areas.
93 Predicting the likelihood of landslide events can help minimize property loss, guide schedule adjustments,
94 improve work safety, and ensure smooth traffic flow during critical periods. Additionally, understanding
95 internal displacements provides engineers with precise data to evaluate the resilience of structures and
96 infrastructure in vulnerable areas, enabling the issuance of prudent warnings.

97 2. Literature Review

98 2.1 Groundwater Levels and the Forecasting of Deep-Seated Displacements

99 Landslide triggers can be attributed to loading, slope geometry, weather conditions, and
100 hydrological conditions (Perkins et al., 2024; Van Natijne et al., 2023; Millán-Arancibia and Lavado-

101 Casimiro, 2023; Jones et al., 2023). Among these, hydrological conditions, especially groundwater levels,
102 have been one of the most critical elements considered in studies related to landslide prediction. Numerous
103 studies have substantiated this point. For instance, research by Take et al. (2015) demonstrated that the
104 distance and velocity of landslides triggered under high-antecedent groundwater conditions are
105 significantly more significant compared to scenarios with drier conditions. Another study has shown that
106 water accumulation at a soil-bedrock contact can develop positive pore water pressures, causing landslides
107 (Matsushi and Matsukura, 2007) (see Figure 1). Moreover, studies on past landslide events have also
108 demonstrated similar findings. ~~example~~Examples of this research include the Tessina landslide in
109 northeastern Italy, where groundwater conditions triggered movement (Petley et al., 2005). Additionally,
110 the study by Keqiang et al. (2015) on water-induced landslides in the Three Gorges Reservoir project area
111 highlights the significant impact of hydrological conditions on the likelihood of such disasters (~~Keqiang~~
112 ~~et al., 2015~~).

113 Similarly, Preisig (2020) developed a groundwater prediction model for analyzing the stability of a
114 compound slide in the Jura Mountains (~~Preisig, 2020~~). Additionally, Srivastava et al. (2020) explored
115 machine learning algorithms to forecast rainfall and established thresholds for landslide probabilities
116 (~~Srivastava et al., 2020~~). Although the research by Srivastava et al. did not directly rely on groundwater
117 levels to predict landslides, it is evident that rainfall, a crucial factor in their study for landslide prediction,
118 also influences hydrological conditions. Therefore, their research further underscores the importance of
119 considering groundwater levels in landslide prediction.

120 The northern slope in the Lushan area of central Taiwan, the region investigated in this study,
121 exhibits significant gravitational slope deformation, making it prone to landslides during typhoons or
122 heavy rainfall events. Lin et al. (2020) conducted in-depth studies on the mechanisms of landslide
123 occurrence based on the geological conditions of the area (~~Lin et al., 2020~~). While successfully providing
124 valuable insights into the evolution of deep-seated gravitational deformations, ~~their research somewhat~~
125 ~~overlooked the importance of hydrological conditions and groundwater levels in landslide formation; their~~
126 ~~study focuses exclusively on employing traditional analytical methods in geological research, such as~~
127 ~~analyzing data from geotechnical instruments and conducting geological borehole analysis.~~

128 Our research aims to adopt a novel approach compared to previous landslide studies at Lushan
129 Mountain by utilizing AI models and metaheuristic optimization algorithms. This research will utilize ~~To~~
130 ~~address the limitations of previous landslide research in the Lushan Mountain area, this study will explore~~
131 ~~using hydrological weather~~ conditions and groundwater levels as inputs for AI models to predict deep-
132 seated displacement, thus aiding in landslide forecasting in this region.

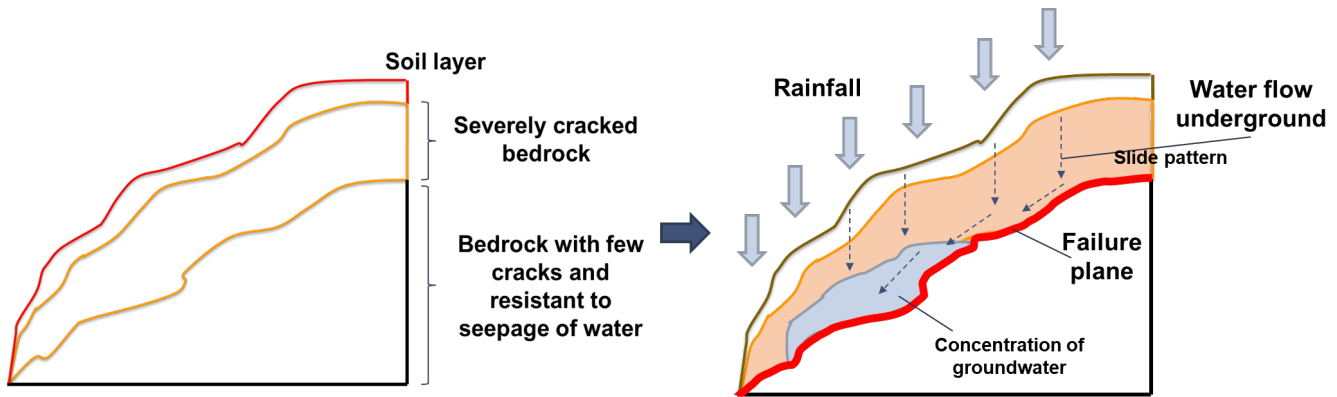


Figure 1. Schematic illustration showing the effects of groundwater on deep-seated slope failure

2.2 Forecasting Slope Displacements: Conventional Methods

Several conventional methods are commonly employed to predict deep slope displacement. These methods primarily involve simulating factors affecting slope stability in landslide-prone areas using data collected from ground-based monitoring devices. An early approach to predicting deep-seated slope movements is geotechnical mapping. This technique characterizes rock and soil's strength, density, and porosity.

For instance, Crosta and Agliardi (2003) analyzed the geology and rock mass behavior using Voight's semi-empirical failure criterion, incorporating time-dependent factors to generate velocity curves that indicate risk levels (Crosta and Agliardi, 2003). Recently, Xu et al. (2018) utilized real-time remote monitoring systems to measure internal stress, deep displacement, and surface strain. This data was used to formulate forecasting models to assess slope stability, particularly in railway construction (Xu et al., 2018). However, a common challenge with this method is the instability and frequent changes in the terrain and geology of landslide-prone areas. This necessitates constant updates to the computational model, which can be time-consuming and labor-intensive.

Moreover, physical-based numerical and laboratory modeling methods, which simulate phenomena at a laboratory scale, are also gaining traction in landslide research. These methods aim to maintain forecasts using various data types while reducing human workload and ensuring high accuracy. For example, Mufundirwa et al. conducted a laboratory study to examine the effectiveness of the inverse velocity model in predicting rock mass destruction resulting from landslides at depths of 2m and 4m along the sliding plane. This study utilized historically recorded data from Asamushi, Japan, and the Vaiont reservoir in Italy (Mufundirwa et al., 2010). Meanwhile, Wu (2010) employed the numerical discontinuous deformation analysis method to simulate a blocky assembly's post-failure behavior, incorporating earthquake seismic data (Wu, 2010). Meanwhile Another study follows this trend by Jiang et al. (2011), who utilized the fluid-solid coupling theory to simulate displacement and capture capturing the interaction between fluid and solid materials (Jiang et al., 2011). However, both numerical models and laboratory modeling methods require substantial effort from researchers. These approaches demand

161 deep expertise and the development of complex models. More importantly, they rely heavily on
162 assumptions during the simulation process and may not accurately reflect real-world conditions, leading
163 to significant errors.

164 Stability analysis is another commonly used method related to physics, which evaluates the forces
165 acting on a slope behavior. Fu and Liao (2010) presented a technique for implementing the non-linear
166 Hoek-Brown shear strength reduction, determining the correlation between normal and shear stress based
167 on the Hoek-Brown criterion (~~Fu and Liao, 2010~~). Subsequently, the micro-units (**microscopic**
168 **components of the rock mass**) instantaneous friction angle and cohesive strength under specific stress
169 conditions are calculated. Although this approach effectively addresses cost and labor issues, it still
170 heavily relies on the ~~researcher's~~ researcher's assumptions and is limited by the ability to utilize only a
171 small portion of data from the research area.

172 However, in landslide studies, monitoring data is constantly updated, generating large volumes daily
173 with a temporal relationship (Peternel et al., 2022; Corominas et al., 2014). ~~Hence, conventional methods~~
174 ~~have shown limited success in handling big data, especially in identifying highly intricate samples that~~
175 ~~require analysis of time series relationships or complex nonlinear associations~~. As previously mentioned,
176 using conventional methods in landslide research presents numerous challenges whenever data changes
177 or gets updated. In contrast, AI models can overcome these difficulties by automatically learning to
178 identify connections between input and output data. AI models can be updated to incorporate additional
179 input variables and handle increasing amounts of data flexibly in response to real-world conditions.
180 Therefore, AI models will be utilized in this research instead of conventional methods.

181 **2.3 Forecasting Slope Displacements: Machine Learning and Deep Learning**

182 In studies employing machine learning and deep learning models for landslide research, a plethora
183 of research utilizes discrete data to train AI models to predict the probability of landslides or to construct
184 maps depicting landslide susceptibility. For instance, Margarint et al. (2013) employed a logistic
185 regression model to predict landslides based on discrete data in four regions of Romania (~~Margarint et al.,~~
186 ~~2013~~). The logistic regression model yielded promising predictions, with an AUC value (area under the
187 curve) ranging between 0.851 and 0.94 for the validation dataset. Subsequently, these results were utilized
188 to construct a map of landslide susceptibility in the study area. In a similar study, Pham et al. (2016) used
189 multiple AI models, including support vector machines (SVM), logistic regression (LR), ~~Fisher's~~ Fisher's
190 linear discriminant analysis (FLDA), Bayesian network (BN), and naïve Bayes (NB), for landslide
191 susceptibility assessment in a region within the Uttarakhand state of India (~~Pham et al., 2016~~). The SVM
192 model yielded the best prediction results among the models used.

193 In addition to discrete data, many landslide studies utilize time series data. When it comes to
194 technical forecasting using time series data, machine learning regression prediction models, such as

195 extreme learning machine (ELM) (Li et al., 2018), least squares support vector machine (LSSVM) (Liu
196 et al., 2019), dynamic neural network (DNN) (Aggarwal et al., 2020), random forests (RFs) (Hu et al.,
197 2021), SVM (Zhang et al., 2021), and Gaussian process regression (GPR) (Hu et al., 2019), have proven
198 highly effective at yielding reliable results. These models also provide scalability and the ability to handle
199 larger datasets. However, it is essential to note that machine learning models are sensitive to the white
200 noise typical of time series features. This can pose challenges in capturing subtle behaviors and complex
201 interrelationships, mainly when data availability is limited (Zhang et al., 2020). Finally, feature
202 engineering (the process of selecting and transforming input variables to enhance the performance of the
203 models) is computationally intensive and labor-intensive, limiting its applicability when rapid forecasting
204 is required.

205 ~~Given that slope profiles and soil parameters are one-dimensional variables, Alongside the~~
206 ~~forementioned machine learning models, a range of neural network models, from simpler ones like~~
207 ~~Artificial Neural Networks (ANN) to more advanced approaches such as Deep Neural Networks (DNNs)~~
208 ~~and CNN can also be employed in research related to landslide (Kumar et al., 2017; Zheng et al., 2022)~~
209 ~~to uncover the relationship between slope stability and input parameters with minimal computational~~
210 ~~overhead (Fu et al., 2022). Notably, CNN models have become increasingly popular and are widely used~~
211 ~~in research related to this disaster. CNN models often yield superior predictive results than other models~~
212 ~~in landslide susceptibility assessment and displacement prediction (He et al., 2024). Additionally, CNN~~
213 ~~models have been used in studies of this disaster. While CNN was initially designed for image processing,~~
214 ~~its input and internal architecture are tailored for two-dimensional matrices, including the convolution~~
215 ~~kernel and feature map. To address the one-dimensional nature of slope profiles and soil physical and~~
216 ~~mechanical parameters, Pei, Meng, & Zhu developed a 1D-CNN model with dynamic inputs to account~~
217 ~~for time-varying trigger factors (Pei et al., 2021). Their approach demonstrated superior performance to~~
218 ~~conventional machine learning models regarding accuracy and robustness. However, it's worth noting that~~
219 ~~this approach has yet to gain widespread adoption.~~

220 Moreover, another research trend in landslide forecasting involves the use of time series deep
221 learning models such as Recurrent Neural Networks (RNN), Long Short-Term Memory (LSTM), and
222 Gated Recurrent Units (GRUs), which use previous information to generate current outputs and provide
223 state feedback (Yang et al., 2019; Xu et al., 2022; Yang et al., 2022; Zhang et al., 2022). These time-series
224 deep learning models can effectively capture patterns of changes over time, making them highly suitable
225 for time-series data in landslide-related studies. However, there has yet to be a comprehensive study that
226 employs a combination of machine learning methods, time-series deep learning, and CNN models to
227 compare and determine the most suitable model for predicting landslide displacement prediction.
228 Therefore, our research aims to address this gap.

229 Another noteworthy research trend involves using AI models to predict landslides based on spatial-
230 temporal data. For instance, Dahal et al. (2024) utilized spatial-temporal data to pinpoint where landslides
231 may occur and predict when they might happen and the expected landslide area density per mapping unit
232 (Dahal et al., 2024). The Ensemble Neural Network employed in this research yielded promising
233 predictions, demonstrating its potential for forecasting landslides in Nepal's areas affected by the Gorkha
234 Earthquake. However, our study only managed to gather temporal data. Consequently, the AI models
235 developed in our research will be trained to learn and forecast time-series data.

236 **2.4 Hybrid metaheuristic optimization algorithm and AI models in landslide prediction**

237 In landslide-related research, numerous studies have employed hybrid models, wherein metaheuristic
238 optimization algorithms optimize the hyperparameters of AI models. For example, Balogun et al. (2021)
239 studied landslide susceptibility mapping in Western Serbia (Balogun et al., 2021). This research collected
240 14 different condition factors to serve as input data for the Support Vector Regression (SVR) model to
241 predict landslide occurrences. The study results indicate that SVR models, with hyperparameters fine-
242 tuned by optimization algorithms such as gray wolf optimization (GWO), bat algorithm (BA), and cuckoo
243 optimization algorithm (COA), all yielded better prediction results compared to using a single model.

244 Hakim et al. (2022) conducted a study utilizing CNN models optimized by the GWO and imperialist
245 competitive algorithm (ICA) for landslide susceptibility mapping from geo-environmental and topo-
246 hydrological factors in Incheon, Korea (Hakim et al., 2022). This research demonstrates that GWO and
247 ICA effectively fine-tuned the CNN model, resulting in a highly accurate landslide susceptibility map.

248 Jaafari et al. (2022) employed an AI model known as the group method of data handling (GMDH)
249 for classification purposes, optimizing it using the cuckoo search algorithm (CSA) and the whale
250 optimization algorithm (WOA). In northwest Iran, they aimed to predict landslides based on various
251 factors, including topographical, geomorphological, and other environmental factors (Jaafari et al., 2022).
252 After training and testing, the GMDH-CSA model produced superior prediction results compared to the
253 GMDH-WOA and the standalone GMDH model.

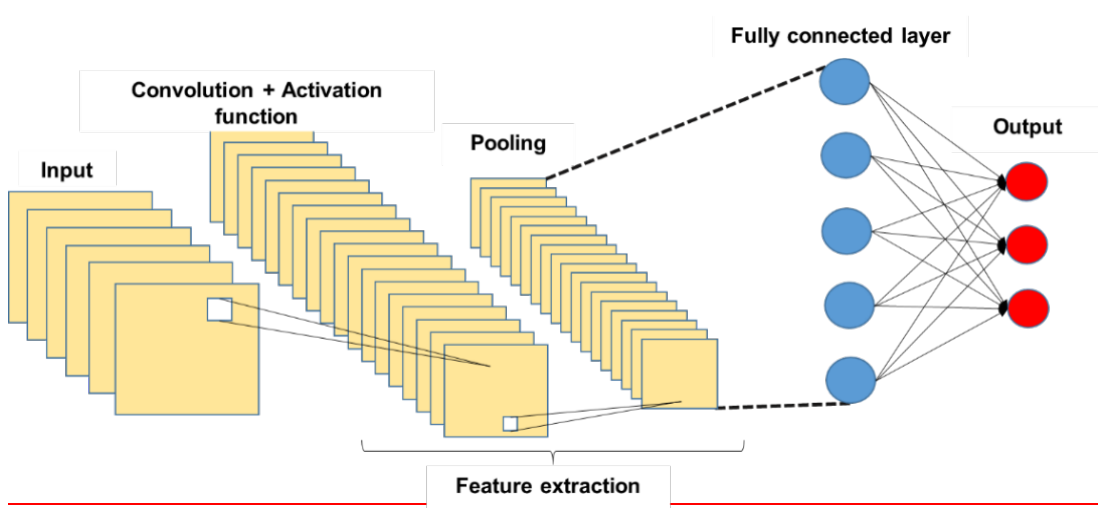
254 It is evident from numerous past studies on landslides that the application of metaheuristic
255 optimization algorithms significantly enhances the predictive effectiveness of AI models. Therefore, this
256 study also incorporates this approach to ensure the model's accuracy in landslide prediction. This study
257 will also employ a recently developed metaheuristic algorithm, including a clustering algorithm. This
258 algorithm is promising in yielding favorable results in fine-tuning hyperparameters for AI models.

259 **3. Methodology**

260 **3.1 Convolutional Neural Networks**

261 In 1998, LeCun introduced a novel type of DNN known as the CNN, specifically designed for
262 processing data with a grid-like structure, such as images. The complex, layered system of CNN facilitates

263 the automated extraction of features without extensive preprocessing, making it ideal for object
 264 recognition, image classification, and segmentation tasks. The detailed mechanism of the CNN model can
 265 be found in Appendix A. The architecture of a typical CNN, as illustrated in Figure 2, comprises an input
 266 layer (to receive image data), followed by hidden layers (including convolutional, pooling, and fully
 267 connected layers), and concludes with the output layers. As depicted in Figure 2, the complexity of CNN
 268 progressively increases from the convolutional layer to the fully connected (FC) layer. This design enables
 269 CNN to recognize relatively simple patterns (lines, curves, etc.) before progressing to capture more
 270 intricate features (faces, objects, etc.), with the ultimate aim of extracting relevant information for accurate
 271 pattern identification.



272
 273 Figure 2. Structure of basic CNN.

274 As illustrated in Figure 3, the convolutional layer is responsible for most computations in the network.
 275 This involves extracting local features from an image using a set of learnable filters known as kernels.
 276 The behavior of the filter in the convolutional layer is influenced by two main factors: stride and padding.
 277 Stride refers to the pixel shift of the filter across the image, while padding aims to preserve information at
 278 the corners. In each iteration, a portion of the image is convolved with a filter to generate a dot product of
 279 pixels within its receptive field. This process is replicated across the entire image to produce a feature
 280 map. The convolution operation is defined as follows:

$$281 \quad C_i = b_i + \sum_{j=1}^{d_i} I_j * F_{ij}, \quad i = 1 \dots d_e \quad (1)$$

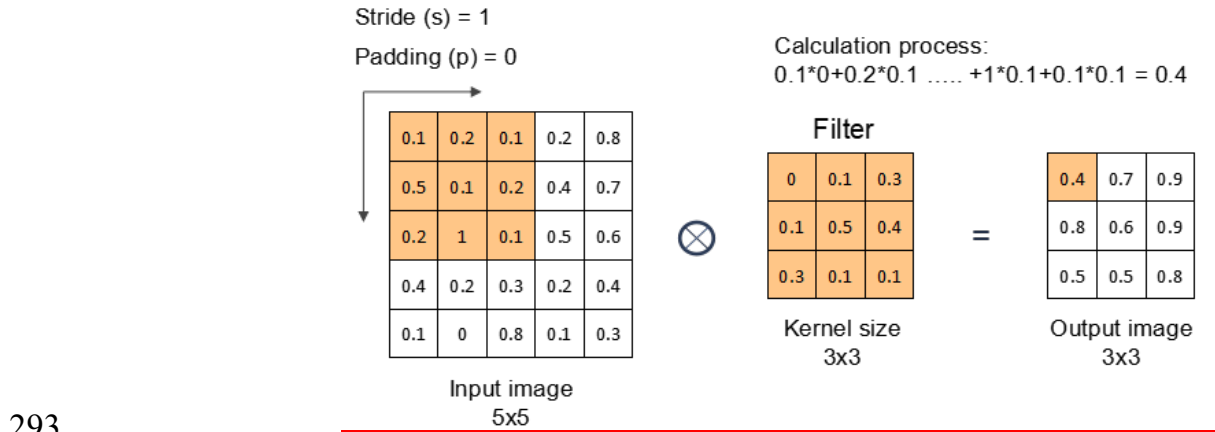
282 where C_i is the output of the convolutional layer or feature map, b_i is the bias, d_i is the depth of input, I_j
 283 is the input image, F_{ij} is the filter, and d_e is the depth of the convolutional layer.

284 The multiplicative operations are usually followed by an activation function (the final element in the
 285 convolutional layer), which introduces nonlinearity and creates intricate mappings between network
 286 inputs and outputs. The activation function can be defined as follows:

$$287 \quad Y_i = f(C_i) \quad (2)$$

288 where, Y_i is the output of the convolutional layer after the activation function, and f is the activation
 289 function.

290 A rectified linear unit ReLU is a nonlinear CNN function with output $f(x) = \max(0, x)$. A ReLU
 291 converts all negative values to zero or returns the original input values if the input exceeds zero. ReLU is
 292 only one of many activation functions; however, it has proven to be the most effective overall.



293
 294 **Figure 3. Processing flow in convolution layer.**

295 Pooling layers after the convolution layer can down-sample feature maps by summarizing features
 296 within the coverage area of a 2-D filter to reduce sensitivity to feature location, thereby improving
 297 resilience to changes in the position of features. Pooling layers also decrease the dimensions of the feature
 298 map, reducing the number of parameters to be dealt with, thereby decreasing computational overhead.
 299 Output dimensions from the pooling layer are computed as follows:

$$300 \frac{c_w - f_w + 1}{s} * \frac{c_h - f_h + 1}{s} * c_n \quad (3)$$

301 where c_n is the number of channels in the feature map and $f_w * f_h$ indicate the width and height of the
 302 filter.

303 Max pooling and average pooling are commonly used in CNN. Max pooling accentuates salient
 304 features by selecting the maximum value within the filter's coverage area. In contrast, average pooling
 305 calculates the mean value within the exact location, providing a representative feature value. Illustrations
 306 of max pooling and average pooling are presented in Figure 4.

307 The final stage of a CNN comprises a series of fully connected (FC) layers. After the convolution
 308 and pooling operations, the feature map is flattened into a one-dimensional vector that connects to the FC
 309 layers, resembling an ANN. FC layers identify specific features, each represented by a neuron. In
 310 regression tasks, each neuron in the FC layer corresponds to a feature contributing to the final numerical
 311 output. The value transmitted by each neuron indicates its significance toward the regression result. FC
 312 layers are designed to predict the best continuous value for the target variable by combining and processing
 313 these neuron outputs. Figure 5 illustrates the structure of an FC layer.

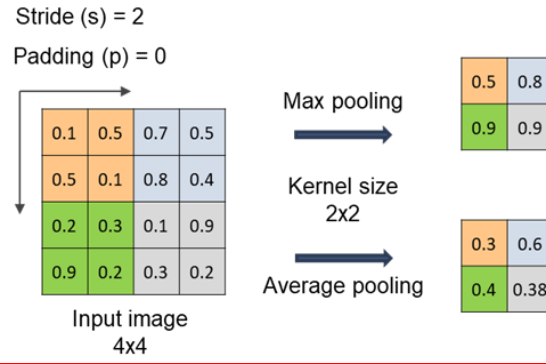


Figure 4. Max Pooling and Average Pooling.

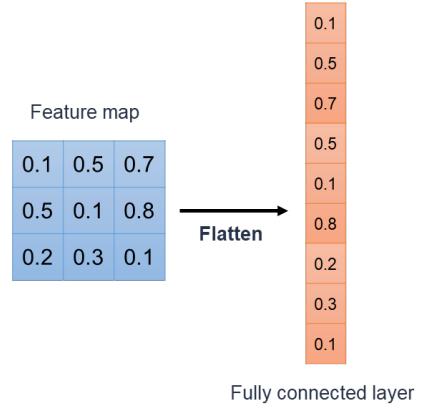


Figure 5. Structure of fully connected layer.

This study will use various CNN models to predict deep-seated slope displacement. The CNN models employed in this research include VGG (Simonyan and Zisserman, 2014), ResNet (He et al., 2016), Inception (Szegedy et al., 2015), Xception (Chollet, 2016), MobileNet (Howard et al., 2017), DenseNet (Huang et al., 2017), and NASNet (Zoph et al., 2018). To clarify, the term "standard CNN models" will refer to models with structures that can be user-defined, while "retrained CNN models" will denote those with architectures that have been researched and developed by other scientists and have been proven to be highly effective.

CNN models are typically used for image processing tasks. However, the input data for this study is in numerical and vector form. Therefore, several transformation steps are required to convert this numerical and vector data into image data suitable for CNN input. Detailed information about these transformation steps can be found in the study by Chou and Nguyen 2023 (Chou and Nguyen, 2023).

3.2 Deep Learning Models for Time Series

RNN was introduced by Elman in 1990 (Elman, 1990). This model makes predictions based on sequential data, crucial for language modeling, document classification, and time series analysis. The architecture of an RNN model can be found in Appendix B.

334 The architecture of an RNN includes an input layer, a hidden layer with a variable number of RNN
 335 cells, and an output layer designed for label identification based on future displacement values. Figure 6
 336 illustrates the structure of simple RNNs.

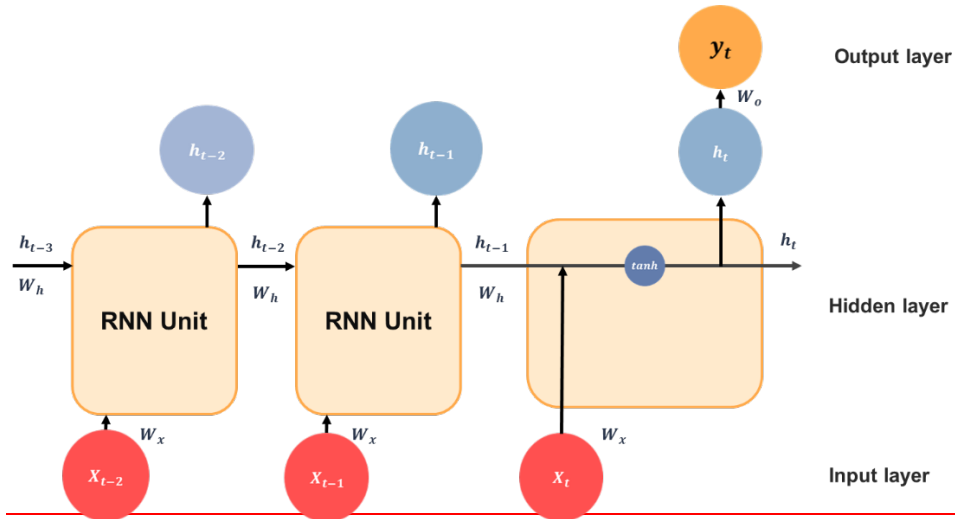
337 Each cell in an RNN acts as a memory cell, which is interconnected to enable the sequential transfer
 338 of time-dependent input information within a sliding window. This makes it possible to consider temporal
 339 correlations between events that may be widely separated in the time dimension. The following formula
 340 presents the hidden unit of standard RNNs at time t :

$$341 \quad h_t = \tanh(W_x * x_t + W_h * h_{t-1} + b) \quad (4)$$

342 where x_t is the input vector at time t ; h_t is the output vectors of hidden units for
 343 time t ; W_x and W_h respectively indicate the input and interconnected weight matrices for the output of the
 344 hidden layer; b is the bias term; and $\tanh()$ represents the hyperbolic tangent activation function, i.e.,

$$345 \quad \tanh(x) = \frac{1 - e^{-2x}}{1 + e^{-2x}}$$

346 capture complex relationships between cells and time sequences effectively. However, as the duration of
 347 dependencies increases, RNN models are susceptible to issues related to vanishing gradients (Bengio et
 348 al., 1994). Therefore, RNNs are well suited to learning time series involving short term dependencies.



349
 350 **Figure 6. Structure of basic RNNs.**

351 In this study, advanced models of RNN, such as LSTM [54] and GRU [55], are also utilized, and
 352 their effectiveness in predicting deep-seated landslides will be compared.

353 3.3 Machine Learning

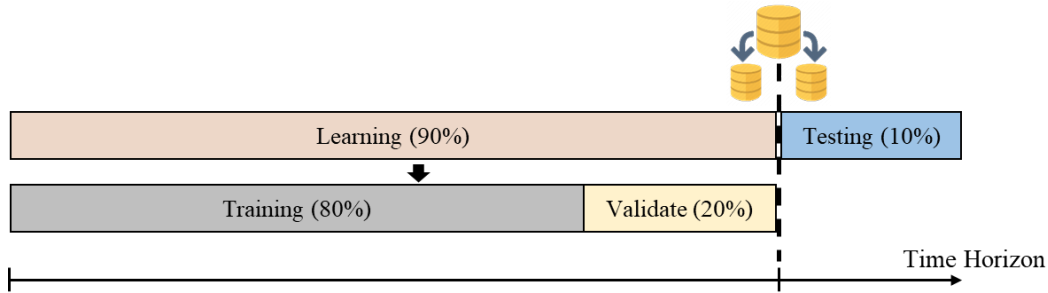
354 In addition to the aforementioned deep learning models, as elucidated earlier, machine learning
 355 models will be employed to predict deep-seated slope displacements in this research. The machine
 356 learning models utilized will encompass the following: linear regression (LR) (Stanton, 2001), ANN
 357 (McCulloch and Pitts, 2021), SVR (Drucker et al., 1996), classification and regression tree (CART)
 358 (Breiman, 1984), radial basis function neural network (RBFNN) (Han et al., 2010), extreme gradient

359 boosting (XGBoost) (Chen; and Guestrin). These machine learning models will be used to make
360 predictions and will be compared with other deep learning models.

361 3.4 Model Validation and Performance Metrics

362 3.4.1 Evaluation and Validation

363 To obtain reliable (i.e., generalizable) evaluation and validation results, it is crucial that the data
364 used for testing does not include the data used for training. Therefore, a dataset must be divided into
365 training, validation, and testing subsets before training the AI model. Training data is used to learn patterns;
366 testing data is used to assess model performance and identify errors; and validation data is used to fine-
367 tune the hyperparameters. In the current study, we opted to refrain from employing cross-validation, which
368 tends to be time-consuming. Instead, we adopted the holdout approach to manage our large dataset with
369 well-represented target variables (Figure 2). A 90:10 ratio is generally used to split datasets into learning
370 and testing data (Di Nunno et al., 2023). When implementing the holdout method during hyperparameter
371 optimization, 20% of the learning data is used for validation, and the remaining 80% is used for training.



372

373

Figure 2. Data are splitting under the proposed Holdout scheme.

374

374 3.4.2 Performance Metrics

375

376

This study utilized four widely recognized performance measures to assess the ~~model's~~ model's effectiveness in prediction accuracy (Chou and Nguyen, 2023). The measures included mean absolute error (MAE), mean absolute percentage error (MAPE), and root mean square error (RMSE).

377

378

379

MAE represents the mean of absolute errors, calculated as the average of the absolute differences between actual and predicted values. Its advantage lies in its simplicity, which provides a straightforward measure of average prediction error. However, a drawback of MAE is its insensitivity to more significant errors, so it may not effectively highlight differences between models when significant errors are present. It is defined as:

382

383

$$MAE = \frac{1}{n} \sum_{i=1}^n |y_i - \hat{y}_i| \quad (1)$$

384

where n is the number of predictions, y_i is the i^{th} forecasted value, and \hat{y}_i is the corresponding i^{th} actual value.

385

386 MAPE quantifies the average absolute error ratio to the actual value derived from the
387 differences between actual and forecasted values. It provides a clear metric in percentage terms,
388 facilitating straightforward interpretation across various datasets. However, MAPE's limitation
389 arises from its sensitivity to zero values in the actual data, which can become undefined or
390 impractical to compute, limiting its utility in scenarios involving zero or near-zero actual values.
391 The expression for MAPE is as follows:

$$392 \quad MAPE = \frac{1}{n} \sum_{i=1}^n \left| \frac{y_i - \hat{y}_i}{y_i} \right| \quad (2)$$

393 where n is the number of predictions, y_i is the i^{th} forecasted value, and \hat{y}_i is the corresponding i^{th}
394 actual value.

395 RMSE represents the square root of the average squared error between actual and forecasted
396 values and is widely used for its ability to indicate the dispersion of errors. This method captures
397 the magnitude and direction of errors, making it practical for assessing overall prediction accuracy.
398 However, RMSE tends to be more sensitive to outliers and significant errors than MAE due to its
399 squaring of errors during computation. This sensitivity can disproportionately affect its evaluation
400 in datasets with extreme values. The expression for RMSE is as follows:

$$401 \quad RMSE = \sqrt{\frac{1}{n} \sum_{i=1}^n (y_i - \hat{y}_i)^2} \quad (3)$$

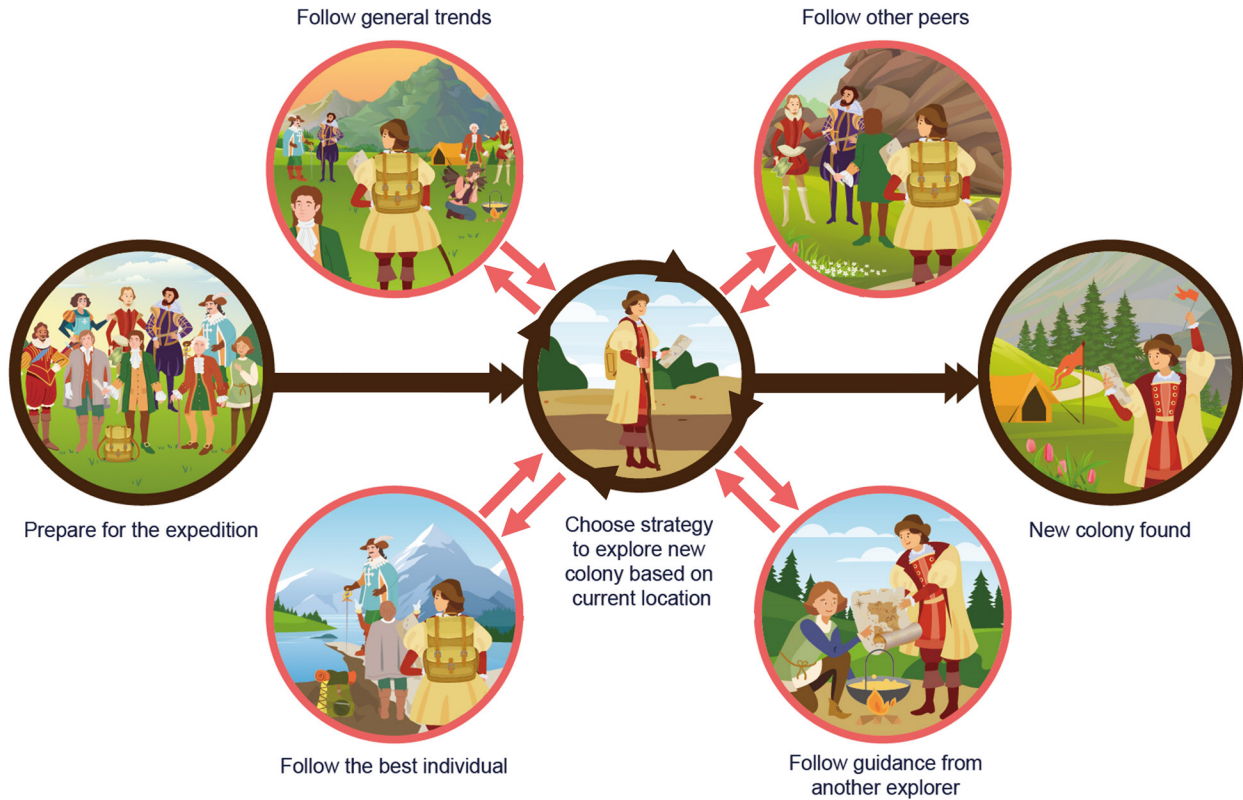
402 where n is the number of predictions, y_i is the i^{th} forecasted value, and \hat{y}_i is the corresponding i^{th}
403 actual value.

404 3.5 Age of Exploration-Inspired Optimizer

405 This study employs a range of AI models to forecast deep-seated displacement in mountainous
406 regions. To enhance the prediction accuracy of these AI models, the study incorporates a novel
407 metaheuristic optimization algorithm known as the Age of Exploration-Inspired Optimizer (AEIO).
408 Developed by Chou and Nguyen in 2024, this algorithm has demonstrated high effectiveness in fine-
409 tuning the hyperparameters of AI models. This algorithm treats each particle in the search domain as an
410 explorer. The movement of particles toward regions with higher fitness values parallels the exploratory
411 activities of the Age of Exploration, where explorers sought ideal locations for establishing colonies. In
412 this study, each particle represents a set of hyperparameters, with the ultimate goal of the search process
413 being to identify the optimal particle or hyperparameter set that minimizes prediction error for AI models.
414 Figure 3 illustrates the AEIO algorithm.

415 The strength of the AEIO algorithm lies in its ability to develop specific strategies for particles based
416 on their positions, enabling faster convergence to the optimal point. Using density-based spatial clustering

417 of applications with noise (DBSCAN) for particle clustering, the AEIO determines whether particles are
 418 in favorable or unfavorable positions, reminiscent of explorers during the Age of Exploration. The
 419 proximity (within clusters) allows explorers to gather information and move toward optimal locations,
 420 thereby enhancing their ability to establish new colonies. In contrast, explorers far apart (outside clusters)
 421 adopt different strategies, relying on limited peer guidance or general trends in their quest for new
 422 territories.



423

424

Figure 3. Illustration of Age of Exploration-Inspired Optimizer

425

426

427

428

429

430

431

432

433

434

435

In each iteration, explorers forecast their next move. If it promises a better position, they relocate. Otherwise, if the new spot is less favorable for colony establishment, they stay put and await the next iteration. The algorithm employs specific mathematical formulas to calculate the movement step of explorers or particles in the AEIO. **The exploratory steps of an explorer in the AEIO algorithm will continuously iterate until the stop condition is satisfied.**

- **Explorers follow general trends**

The explorer choosing this movement type will calculate the distance from their location $x_{i,d}(t)$ to the center of all other explorers ($Meanvl_d(t)$), then attempt to move towards that central point in the hope of finding a better location with the potential to establish a new colony. The following formula determines the explorer's position after the movement:

$$x_{i,d}(t + 1) = x_{i,d}(t) + \alpha * (Meanvl_d(t) - x_{i,d}(t)) \times rand(0,1) \times R \quad (4)$$

$$436 \quad Meanvl_d(t) = \frac{x_{1,d}(t)+x_{2,d}(t)+\dots+x_{n_{Pop},d}(t)}{n_{Pop}} \quad (5)$$

437 where $d = 1,2, \dots, D$; D is the number of dimensions; $i = 1,2, \dots, n_{Pop}$; n_{Pop} is the total number of
 438 explorers; $t = 1,2, \dots, MaxIt$ is the number of iterations; $MaxIt$ is the maximum value of iteration; α is a
 439 parameter for adjusting the particle's movement toward the centroid position (usually equals 3).
 440 $Meanvl_d(t)$ is the centroid of all particles in dimension d . $rand(0,1)$ is the random number in the range
 441 $[0,1]$. R : a number that equals 1 or 2 depending on the value of $rand(0, 1)$ per the equation. $R =$
 442 $round(1 + rand(0,1) \times 1)$, $x_{i,d}(t)$ is the location of particle i in iteration t , $x_{i,d}(t + 1)$ is the location
 443 of particle i in iteration $(t + 1)$.

444 • **Explorers follow three other peers**

445 Explorers employing this movement method will calculate the average position of three randomly
 446 selected other explorers $\left(\frac{x_{1,d}(t)+x_{2,d}(t)+x_{3,d}(t)}{3}\right)$ and then move toward this newly calculated average
 447 position. The explorer's new position is computed using the following formula:

$$448 \quad x_{i,d}(t + 1) = x_{i,d}(t) + \left(\frac{x_{1,d}(t)+x_{2,d}(t)+x_{3,d}(t)}{3} - x_{i,d}(t)\right) \times rand(0,1) \times R \quad (6)$$

449 where: $x_{1,d}(t)$, $x_{2,d}(t)$ and $x_{3,d}(t)$ are three random explorers in dimension d at iteration t , $d = 1,2, \dots, D$;
 450 D is the number of dimensions; $i = 1,2, \dots, n_{Pop}$; n_{Pop} is the total number of explorers; $t = 1,2, \dots, MaxIt$
 451 is the number of iterations; $MaxIt$ is the maximum value of iteration.

452 • **Explorers follow the best one**

453 According to this strategy, the explorer $(x_{i,d}(t))$ will move closer to the position of another explorer
 454 currently holding the best position $(Best_d(t))$, as determined by the following formula:

$$455 \quad x_{i,d}(t + 1) = x_{i,d}(t) + (Best_d(t) - x_{i,d}(t)) \times rand(0,1) \times R \quad (7)$$

456 where: $Best_d(t)$ represents the position of the particle with the best fitness in dimension d at iteration t ,
 457 the parameters d and t hold the same significance as defined in Equation 10.

458 • **Explorers follow guidance from another one**

459 Explorers in favorable positions with access to information can execute this movement strategy. In
 460 this scenario, explorers $(x_{i,d}(t))$ will consult with ~~each other~~ another explorer. The consulted explorer will
 461 compare their direction and distance to the best individual, who holds the most favorable position
 462 $(Best_d(t))$ and guide the inquirer. This algorithm assumes that the inquirer can be any explorer, i.e., a
 463 random explorer $(x_{1,d}(t))$. The following formula describes how to calculate the new position of the
 464 explorer following this strategy:

$$465 \quad x_{i,d}(t + 1) = x_{i,d}(t) + (Best_d(t) - x_{1,d}(t)) \times rand(0,1) \times R \quad (8)$$

466 where: $x_{1,d}(t)$ is a random explorer in dimension d at iteration t . the parameters d and t hold the same
 467 significance as defined in Equation 10.

468 • **Crowd control mechanism**

469 To enhance the efficiency of AEIO in transitioning between exploration and exploitation, a
470 mechanism is employed to adjust the parameters of DBSCAN throughout each cycle, according to the
471 following formula:

$$472 \quad \varepsilon_d = \left(0.1 + \frac{t}{MaxIt}\right) \times (Meanvl_d(t) - Best_d(t)) \quad (9)$$

$$473 \quad MinPts = round\left(1 + \frac{t}{MaxIt} \times 10\right) \quad (10)$$

474 The exploratory steps in the AEIO algorithm begin by classifying positions using the DBSCAN
475 algorithm. Subsequently, the explorers update the crowd control mechanism according to equations (13)
476 and (14), and move according to various strategies defined by equations (8), (10), (11), and (12). This
477 process is conducted iteratively until the maximum number of iterations is reached.

478 To fine-tune the hyperparameters of AI models, the AEIO algorithm treats each hyperparameter as
479 a variable. Furthermore, the objective function of the AEIO algorithm seeks to minimize the prediction
480 error of AI models, which is quantified by an evaluation metric (MAPE). Figure 4 presents a flowchart
481 illustrating the process by which the AEIO algorithm aids in fine-tuning hyperparameters for AI models.

482 **3.6 Experiment Setup**

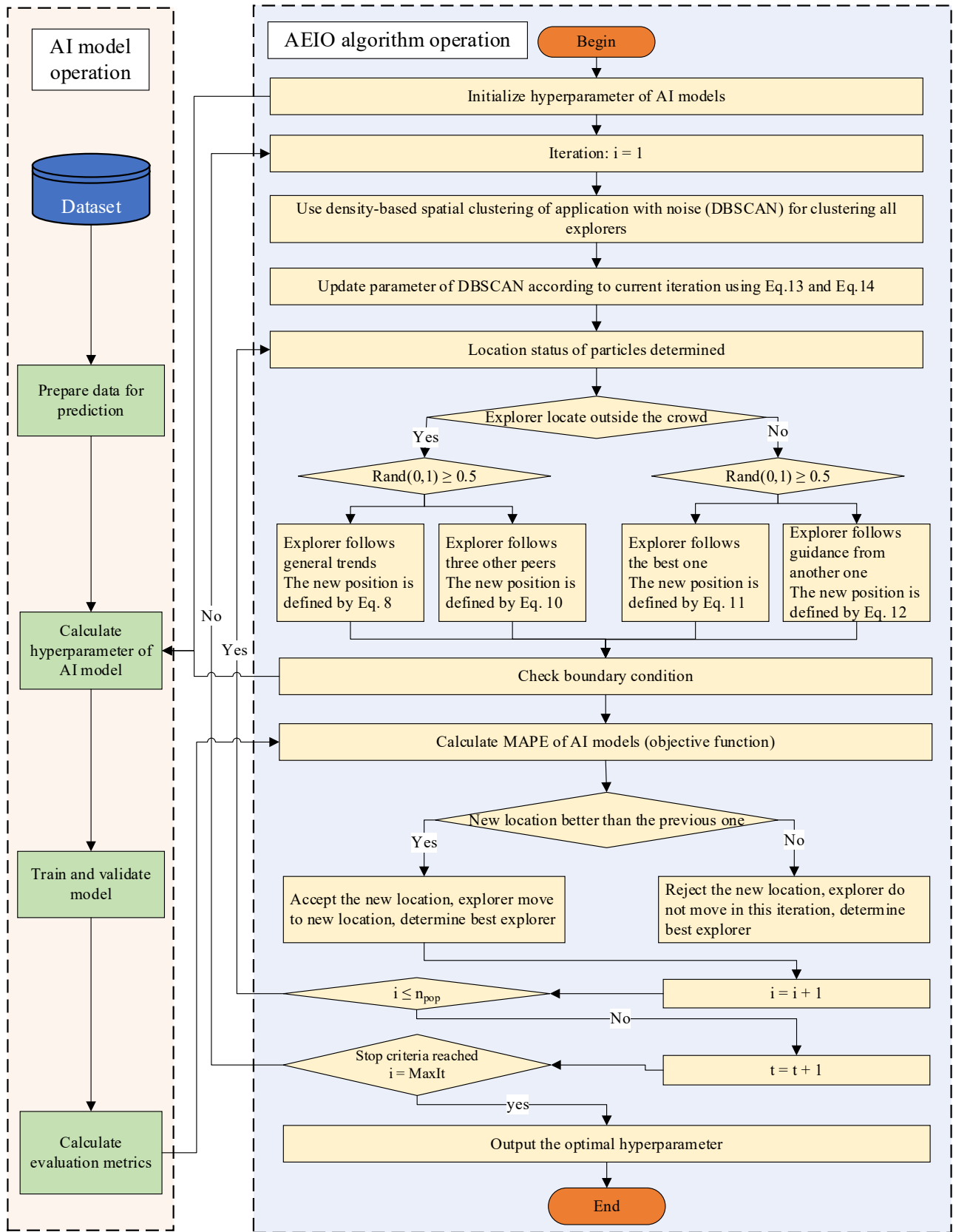
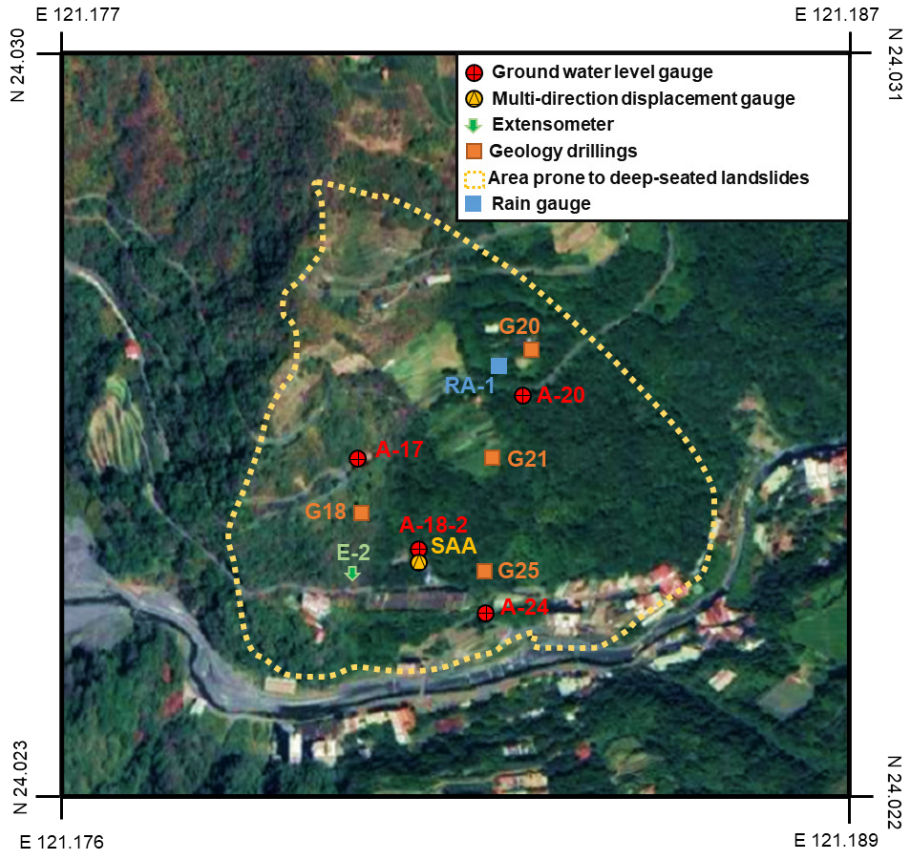


Figure 4. Flowchart of the fine-tuning process of AI models by the AEIO algorithm

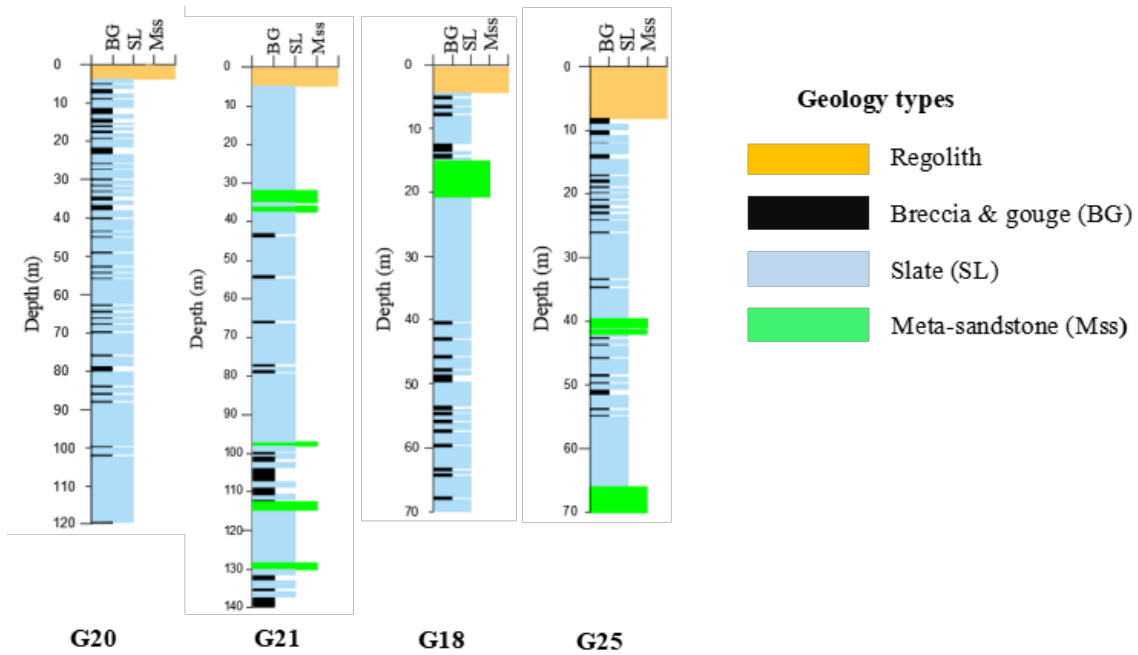
3.6.1 Research Area



487
488
489

Image source: Imagery ©2022 CNES/Airbus, Maxar Technologies, Map data ©2022 Google

Figure 5. Locations of measurement devices



490
491

Figure 6. Illustration of geological drilling survey

492 The current study focuses on the northern slope of Lushan hot spring in Ren'ai Township, Nantou
493 County (Figure 5), with Nenggao Mountain to the east, Hehuan Peaks to the north, Zhuoshe Mountain to
494 the south, and Puli Basins to the west. The terrain features rugged mountain ranges, youthful valleys, and

495 notable river erosion (Lee and Chi, 2011). Lushan Hot Springs is located below the hill, and the main
496 access roads for nearby settlements and hot spring sites include Provincial Highway 14 and County
497 Highway 87.

498 In an early study of deep landslides in this area, [Lin et al.](#) (Lin et al. (2020) reported that the Lushan
499 slope exhibits large-scale deep-seated gravitational slope deformation, characterized by a steep scarp, a
500 gently inclined head, and a curving river at its base. Figure 6 illustrates the geological details of the
501 research area and shows the distribution of four survey boreholes (G20, G21, G18, and G25) along the
502 slope. Regolith, slate, and meta-sandstone are three distinct lithological units revealed through drilling.
503 Additionally, the study by Lin et al. identified the depths of failure planes in these survey boreholes.
504 Specifically, boreholes G18 and G25 did not record any failure planes, while boreholes G20 and G21
505 recorded failure planes at depths of 85 meters and 106 meters, respectively. These failure planes were
506 identified based on inclinometer data from the corresponding study (Lin et al., 2020).

507 Initially, the thickness of the topmost regolith layer was found to be less than 10 meters. Secondly,
508 slate predominated, exhibiting a notable presence with sporadic evidence of weathering that resulted in
509 brecciated patterns. This composition frequently broke into breccia and gouges, particularly along
510 cleavage planes and thin shear zones, indicating its susceptibility to collapse. This geological layer is
511 identified as the area's primary cause of landslide risk. Finally, meta-sandstone appeared intermittent
512 compared to the more prevalent lithological units, characterized by its fragility and fractures and occurring
513 less frequently in the drilled samples.

514 Previous research has detected signs of brittle deformation in the area. These indications include
515 chevron folds within cleavages, visible cracks, and intricate jigsaw puzzle-like patterns at the head of the
516 rock formations. Overturned and flexural toppling cleavages are prevalent towards the toe of the slope.
517 Additionally, kink bands are observable on ~~cleavages fractures that have recently undergone~~ recently
518 [undergoing](#) flexural folding along the eastern boundary. Notably, horizontal cleavages near the toe region
519 also exhibit inter-cleavage gouges. [Further details on this geological information can be found in the study](#)
520 [by Lin et al. \(2020\).](#) These instances highlight the potential for significant geological changes and
521 landslide risk in this region.

522 3.6.2 Data Collection and Preprocessing

523 In this study, hourly data of deep-seated displacement and groundwater level were collected by the
524 Department of Civil Engineering, College of Science and Technology, at the National Chi Nan University
525 research group over eight years from July 2009 to June 2017, yielding 68,317 data points. The installation
526 time points and locations are presented in Table 1 and Figure 5, [respectively](#).

527 The data used in this study were collected using an in-hole telescopic gauge (E-2), a multidirectional
528 shape acceleration array sensor (SAA) with an underground displacement gauge, and four groundwater

529 level gauges (A-17, A-18-2, A-20, and A-24). The transmission, storage, and processing of data are
 530 described in detail in the research of [Lau et al. in 2023](#) Lau et al. (2023).

531 The operation of the in-hole extensometer entailed the installation of a borehole through the sliding
 532 surface. One end of a steel cable was anchored at the bottom, and a displacement gauge was placed at the
 533 free end to measure deformations automatically. The fixed stops for E-2 and SAA were situated at depths
 534 of 70 meters and 40 meters below the surface, respectively. In addition to groundwater level data,
 535 information regarding significant rainfall events in this area was also measured and is presented in Table
 536 2.

537 Table 1. Device installation timepoints

Year	2008	2009	2010	2011	2012	2013	2014	2015	2016	2017
Groundwater level gauge	A-17									
	No data						A-18-2			
	No data		A-20							
	No data		A-24							
Extensometer	No data		E-2							
	No data				SAA					

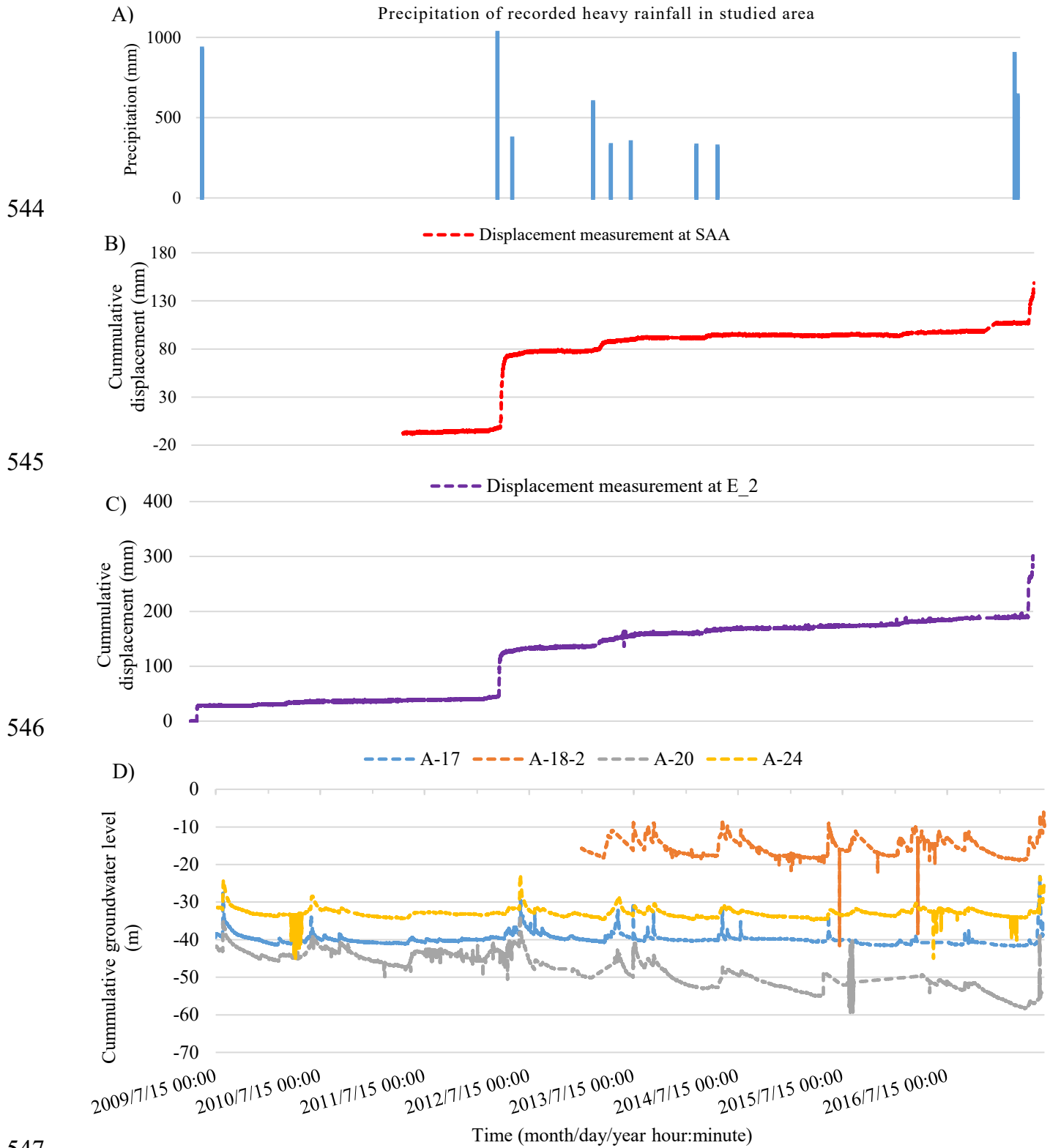
538

539 Table 2. Heavy rainfall events in the study area

No.	Rain onset (month/day/year hour: minute)	Rain end time (month/day/year hour: minute)	Accumulating rainfall (mm)	Drop rain hour (hr)	Event
1	7/17/2008 14:00	7/19/2008 21:00	418	55	Kameiji typhoon
2	9/11/2008 16:00	9/15/2008 12:00	943.5	92	Pungentmusc typhoon
3	9/28/2008 1:00	9/30/2008 10:00	523.5	57	Rose honey typhoon
4	8/4/2009 3:00	8/12/2009 20:00	931	209	Mopull typhoon
5	6/8/2012 13:00	6/17/2012 16:00	1029	219	Torrential rain
6	7/30/2012 7:00	8/3/2012 11:00	370	100	Supull typhoon
7	5/10/2013 16:00	5/25/2013 1:00	597	345	Torrential rain
8	7/12/2013 19:00	7/15/2013 23:00	330	76	Suprofit typhoon
9	9/20/2013 22:00	9/23/2013 18:00	347	68	Usagi typhoon
10	5/9/2014 5:00	5/22/2014 3:00	326.5	310	Torrential rain
11	7/22/2014 14:00	7/24/2014 0:00	321.5	34	Madham typhoon
12	6/1/2017 11:00	6/4/2017 21:00	897	82	Torrential rain
13	6/11/2017 17:00	6/19/2017 3:00	638.5	178	Torrential rain

540 Based on the collected data, analyses have examined the correlation between groundwater levels
 541 and deep-seated displacement at Lushan Mountain. To observe this correlation, [graphs illustrating the](#)

542 precipitation of recorded heavy rainfall (Figure 7A), variations in displacement (Figure 7B and Figure
543 7C), and groundwater levels (Figure 7D) over time have been plotted.



547
548 **Figure 7. Unified timeline visualization of data in this study.**

549 **A) Precipitation of recorded heavy rainfall in the studied area; B) Measured displacements from extensometer SAA C)**
550 **Measured displacements from extensometer E_2; D) Groundwater levels at stations A-17, A-18-2, A-20, and A-24.**

551 The graphs above show that the displacement values at both stations often exhibit significant
552 increases coinciding with periods of pronounced fluctuations in groundwater levels. Specifically, in June
553 2012, there was a notable surge in groundwater levels attributed to heavy rainfall from **June 8, 2012, to**
554 **June 17, 2012**, totaling 1029 mm over 219 hours (as indicated in Table 2 and **Figure 7A**). The abnormal
555 rise in groundwater levels caused a structural alteration in the area's soil, consequently amplifying deep-
556 seated displacement at both stations, namely E_2 and SAA, as evidenced in **Figure 7B** and **Figure 7C**.

557 Similar events occurred in November 2017. Heavy rainfall totaling 638.5 mm over 178 hours during
558 this period also caused a sudden alteration in groundwater levels, resulting in significant deep-seated
559 displacement. Through comparison, it is apparent that there were up to 13 instances of anomalous heavy
560 rainfall during the study period. However, not every example of heavy rain resulted in significant
561 fluctuations in groundwater levels, leading to substantial displacement. Hence, data regarding
562 groundwater level elevation will be used to predict deep-seated landslides rather than rainfall data.

563 In addition to groundwater level data, weather factors such as temperature and humidity are also
564 utilized as input data for the prediction model. **This study includes temperature as an input variable for AI**
565 **models to predict deep-seated displacement due to its impact on soil structure. Elevated temperatures can**
566 **cause thermal expansion of soil particles, which can increase pore water pressure and reduce effective**
567 **frictional resistance forces (Pinyol et al., 2018). Additionally, previous research has shown a relationship**
568 **between temperature and the likelihood of landslides in clay-rich soils, which are also present in the**
569 **geological composition of Lushan Mountain (Shibasaki et al., 2017; Loche and Scaringi, 2023).These**
570 **factors significantly impact the soil structure and can trigger substantial displacement or landslides.**

571 This study collected groundwater level and displacement data on-site using sensors. Furthermore,
572 temperature and humidity data were obtained from the website <https://power.larc.nasa.gov>. This dataset
573 is part of the Prediction of Worldwide Energy Resource (POWER) project, developed by the National
574 Aeronautics and Space Administration (NASA) of the United States. **The POWER solar data derives from**
575 **satellite observations, which are used to infer surface insolation values. Meteorological parameters are**
576 **sourced from the Modern-Era Retrospective analysis for Research and Applications, Version 2 (MERRA-**
577 **2) assimilation model. The primary solar data is available with a global resolution of 1° x 1°**
578 **latitude/longitude, while the meteorological data is provided at a finer resolution of ½° x ⅝°**
579 **latitude/longitude. Users can download the data hourly, daily, or monthly through this website.**

580 Table 3 displays the input and output variables for AI models to predict deep-seated displacement at
581 Lushan Mountain. Two datasets will be generated: one for predicting displacement at the E_2 station and
582 another for indicating displacement at the SAA station. Table 4 outlines the number of data points for each
583 dataset and illustrates how the data is divided into training and testing sets.

584 Table 3. Input and output variables of a model predicting deep-seated displacement.

	Attributes group	Attributes	Variable ID	Dataset of E_2 station	Dataset of SAA station
Output variables	Deep-seated displacement measures	Displacement extensometer at station E_2 (mm)	Y1	✓	-
		Displacement extensometer at station SAA (mm)	Y2	-	✓
Input variables	Groundwater level data	Groundwater level at station A-17 (m)	X1	✓	✓
		Groundwater level at station A-18-2 (m)	X2	✓	✓
		Groundwater level at station A-20 (m)	X3	✓	✓
		Groundwater level at station A-24 (m)	X4	✓	✓
	Weather data	Temperature at 2 meters (°C)	X5	✓	✓
		Specific humidity at 2 meters (g/kg)	X6	✓	✓

585 Table 4. Number of data points

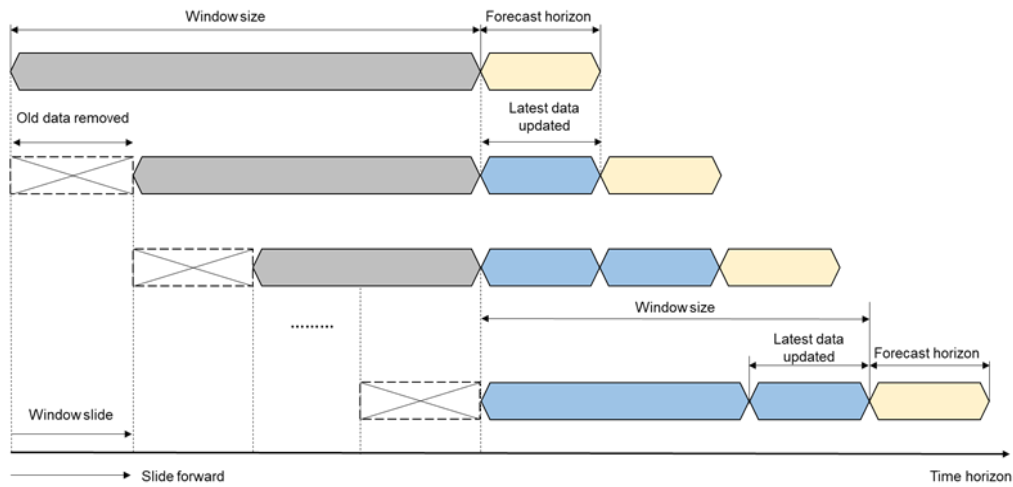
Quantity of data points	Dataset of the E-2 station	Dataset of SAA station
Total data samples	68312	51679
Count of training samples (90% of the total sample)	61477 (2009/07/15-2016/09/07)	46523 (2011/07/13 – 2016/11/16)
Count of testing samples (10% of the total sample)	6835 (2016/09/07-2017/06/20)	5156 (2016/11/16-2017/06/20)

586 **3.6.3 Data Preprocessing**

587 Firstly, the data in this study will undergo a normalization process to scale all features to a consistent
588 range (typically between 0 and 1). This step is essential to ensure that the model considers the importance
589 of each feature, thereby enhancing overall prediction accuracy (Han et al., 2006).

590 In the current study, the sliding window technique is implemented after data normalization to
591 organize data according to a specific time frame. This involves using historical data from previous steps
592 to predict the output for subsequent steps (Chou and Ngo, 2016). The forecasting horizon refers to the
593 length of time into the future for which output forecasts are made.

594 The basic process of the sliding window technique is illustrated in Figure 8. To train AI models, this
 595 study opts for a window size of one week (equivalent to 168 hours). This fixed window size is utilized
 596 exclusively for single AI models. Subsequently, the hybrid model's AEIO algorithm and other
 597 hyperparameters will fine-tune the window size to determine the most suitable settings.



598
 599 **Figure 8.** Sliding window technique

600 This study focuses on predicting deep displacement values at two distinct time intervals: 1 day ahead
 601 (+24 hours) and seven days ahead (+168 hours). These forecast horizons are strategically chosen to
 602 provide timely information, enabling management departments to make accurate decisions regarding
 603 evacuating people and assets from areas prone to landslides.

604 Specifically, for valuable assets and machinery that require time for relocation from landslide-prone
 605 areas, having advance knowledge of the landslide event one week ahead of relocation is crucial.
 606 Furthermore, for humans, animals, or other assets that can be evacuated more swiftly, predicting the
 607 landslide one day in advance is sufficient to ensure safety.

608 The predicted outputs are quantified in mm/day, facilitating decision-making for administrators
 609 according to the TGS-SLOPEM106 standard (Ruitang et al., 2017). Table 5 outlines suggested actions
 610 corresponding to different degrees of deep displacement as per the TGS-SLOPEM106 standard issued by
 611 the Taiwan government.

612 Table 5. Recommendations are taken from TGS-SLOPEM106 for addressing displacement values in the
 613 early stages of deep sliding.

Classification of the displacement value	Attention value	Warning value	Action value
Corresponding displacement value	2 mm/month	0.5 mm/day	10 mm/day

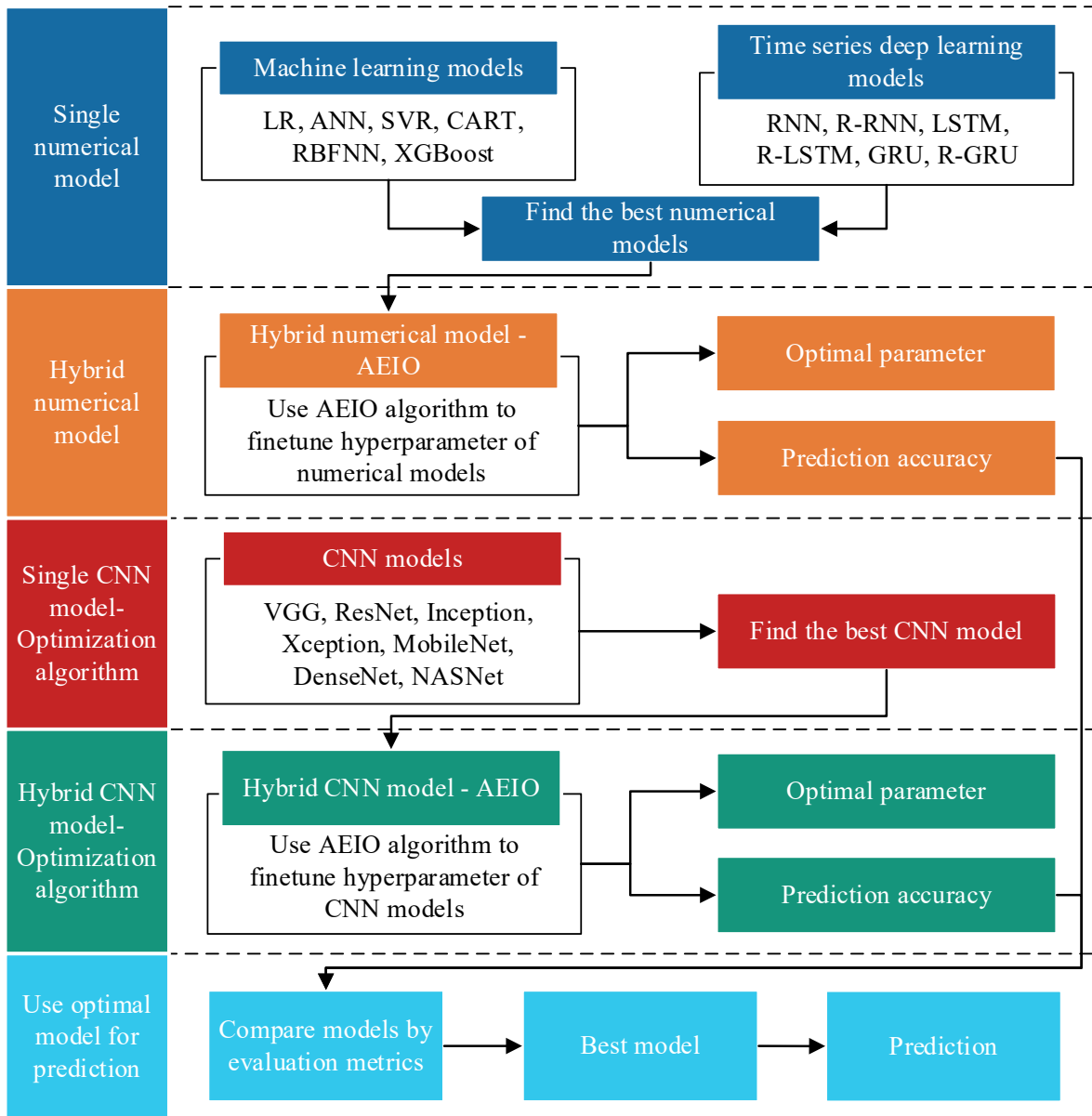
Classification of the displacement value	Attention value	Warning value	Action value
Condition of slopes	The slope started to slip or slowly move	The hill is undergoing constant-velocity descent.	The rate of slope movement is increasing, elevating the risk of collapse.
Recommendations on monitoring activities	- Inspect the monitoring system for any irregularities and consider increasing the frequency of visual inspections	- Enhance the frequency of the automated monitoring system	- Implement a rigorous monitoring system frequency
Countermeasures	- Conduct a slope stability investigation and assessment - Develop a reinforcement and improvement plan to enhance slope stability	- Execute emergency slope reinforcement procedures - Develop an emergency response plan for individuals and vehicles within the landslide area	- Evacuate people and vehicles from the landslide area

614 **4. Model Establishment and Analysis Results**

615 **4.1 Model Establishment**

616 Predicting deep-seated **displacement landslides** at Lushan Mountain is undoubtedly highly
617 challenging, given that such landslides depend on numerous factors. Therefore, multiple methods will be
618 employed simultaneously to identify the optimal AI model for prediction. These methods include single
619 machine learning, time series deep learning, CNN, and hybrid models...

620 This study will conduct a testing process to systematically identify the optimal model capable of
621 accurately predicting deep-seated landslides. An illustration of this process can be found in **Figure 9**.
622 Initially, the study will sequentially employ various single numerical AI models, such as machine learning
623 models (LR, ANN, SVR, CART, RBFNN, XGBoost) and time series deep learning models (RNN, R-
624 RNN, LSTM, R-LSTM, GRU, R-GRU), to forecast displacement.



625

626 **Figure 9.** Diagram depicting the steps of choosing the optimal AI model to predict deep-seated **landslide**

627

displacement

628

Subsequently, the model with the highest prediction accuracy will be selected for integration with the AEIO algorithm, forming a hybrid model. In this hybrid model, the hyperparameters of the best numerical AI model will be fine-tuned by the AEIO algorithm to enhance prediction accuracy.

631

In addition to the numerical AI models, this study employs individual CNN models for predicting deep-seated displacement. Subsequently, similar to the approach above, the best CNN model with the highest displacement prediction capability will be fine-tuned by the AEIO algorithm within a hybrid model. In the final step, a comparison process between the two hybrid models— one comprising the best numerical model and the other involving the best CNN model fine-tuned by AEIO— will be conducted to select the optimal model for this study.

637

4.2 Analysis Results

638 This section will present the experimental results of the steps outlined in Figure 9, along with relevant
 639 metrics and analysis.

640 4.2.1 AI Models

641 a. Machine Learning Models

642 Initially, single machine learning models will be employed to predict deep-seated displacement. In
 643 this phase, machine learning models will utilize default hyperparameters, as detailed in [research of Chou
 644 and Nguyen's research in 2023](#) Chou and Nguyen (2023). The prediction results of these models at both
 645 E-2 and SAA stations are displayed in Table 6. These results show that most machine learning models
 646 demonstrate a relatively good predictive capability for displacement, particularly the XGBoost model,
 647 which exhibits MAPE values ranging from 8.14% to 9.58%. Following closely, CART also produces
 648 favorable prediction results, with MAPE ranging from 8.53% to 9.76%. Regarding prediction accuracy,
 649 XGBoost and CART models outperform LR, ANN, SVR, and RBFNN models.

650 Table 6. Performance results of machine learning models for predicting deep-seated displacement.

Model	MAPE (%)		MAE (mm)		RMSE (mm)		Time (s)	
	1-day-ahead	7-day-ahead	1-day-ahead	7-day-ahead	1-day-ahead	7-day-ahead	1-day-ahead	7-day-ahead
E-2-station								
LR	10.70	11.22	22.61	21.32	28.17	31.96	0.0001	0.003
ANN	12.31	13.31	22.19	24.92	26.56	32.54	129.80	212.83
SVR	12.46	12.47	21.98	22.56	26.27	28.05	162.55	174.44
CART	8.53	8.67	15.67	16.87	25.16	27.81	1.50	2.57
RBFNN	15.13	15.19	23.81	22.56	28.42	31.96	2.32	4.10
XGBoost	8.14	8.36	14.80	14.68	23.07	23.92	1.58	3.28
SAA-station								
LR	11.18	12.11	11.51	11.64	17.26	16.07	0.01	0.01
ANN	10.91	10.93	9.43	10.45	16.55	15.92	116.78	190.69
SVR	10.55	10.94	10.87	9.18	15.64	13.42	136.01	346.30
CART	10.57	10.76	7.11	7.30	13.51	10.63	0.91	1.59
RBFNN	14.51	14.95	11.38	12.68	17.13	19.06	4.20	8.76
XGBoost	9.17	9.58	8.43	7.83	16.36	16.97	1.12	2.29

651 Moreover, the results in Table 6 also indicate that there is not a significant difference in the prediction
 652 errors of the machine learning models at both E-2 and SAA stations, as the error values for both stations
 653 are nearly equal across all machine learning models. Regarding the running time, the LR model
 654 demonstrates the shortest duration, ranging from 0.001 to 0.1 seconds for all runs. However, the prediction

655 accuracy of this model could be higher, as mentioned earlier. In this case, the machine learning model
 656 with the longest running time is SVR, ranging from 136.01 to 346.3 seconds. This, combined with the low
 657 MAPE score, indicates that the SVR model operates inefficiently with the dataset in this study. After
 658 reviewing the results of the machine learning models in this section, it is observed that XGBoost is the
 659 most suitable machine learning model for predicting deep-seated landslides, exhibiting both high
 660 prediction accuracy and a short running time. ~~The following section will compare this model with the best
 661 time series deep learning model to select the optimal numerical model for fine-tuning.~~

662 b. Time series deep learning models

663 Similar to the machine learning models, in this section, the time series deep learning models will
 664 also be trained with default hyperparameters, as found in the ~~research of Chou and Nguyen's research in
 665 2023~~ Chou and Nguyen (2023). The performance results of these models are shown in Table 7. Overall,
 666 akin to the machine learning models, the time series deep learning models also demonstrate fairly good
 667 prediction accuracy, especially the best model - R-GRU model, with MAPE ranging from 7.95 to 9.13%.

668 The performance of the R-GRU model surpasses that of the GRU model because the R-GRU model
 669 learns patterns from time series data in both forward and backward directions on the timeline, thereby
 670 capturing more patterns. Furthermore, the R-GRU model produces significantly better prediction results
 671 with a more complex learning mechanism than other time series deep learning models. However, due to
 672 its complex operational mechanism, the R-GRU model also requires more processing time than other time
 673 series deep learning models. From the results of Table 7, it is observed that the operating time of the R-
 674 GRU model ranges from 79.81 to 212.75 seconds.

675 From the conducted analyses, R-GRU has been identified as the best time series deep learning model,
 676 owing to its excellent prediction performance. Compared to the best machine learning model, XGBoost
 677 (with MAPE ranging from 8.14% to 9.58%), the R-GRU model (with MAPE ranging from 7.90 to 9.13%)
 678 demonstrates higher prediction accuracy. Therefore, the R-GRU model will be chosen as the best
 679 numerical AI model. ~~R-GRU will undergo fine-tuning in the following section using the AEIO algorithm,
 680 further enhancing this model's accuracy.~~

681 Table 7. Performance results of time series deep learning models for predicting deep-seated displacement

Model	MAPE (%)		MAE (mm)		RMSE (mm)		Time (s)	
	1-day-ahead	7-day-ahead	1-day-ahead	7-day-ahead	1-day-ahead	7-day-ahead	1-day-ahead	7-day-ahead
E-2-station								
RNN	12.72	12.92	23.61	24.75	31.18	29.62	83.24	177.53
R-RNN	12.31	12.84	22.88	21.97	30.20	34.42	91.47	114.33
LSTM	8.42	8.57	17.87	16.31	21.41	22.98	123.10	151.91

Model	MAPE (%)		MAE (mm)		RMSE (mm)		Time (s)	
	1-day-ahead	7-day-ahead	1-day-ahead	7-day-ahead	1-day-ahead	7-day-ahead	1-day-ahead	7-day-ahead
R-LSTM	8.13	8.75	16.63	17.84	22.85	24.67	148.56	161.14
GRU	8.43	10.15	16.06	19.38	22.46	26.75	141.50	164.26
R-GRU	7.90	8.16	15.09	15.69	20.84	23.32	156.97	172.96

SAA-station

RNN	11.92	13.98	17.61	12.65	25.71	23.19	36.77	60.31
R-RNN	14.60	14.73	18.77	13.85	26.19	24.97	49.26	59.06
LSTM	10.64	10.94	12.73	12.25	29.21	29.57	62.84	113.76
R-LSTM	10.14	10.35	11.77	11.60	26.10	27.48	70.94	87.48
GRU	9.32	9.28	18.05	18.11	25.26	22.41	69.56	211.77
R-GRU	8.03	9.13	18.84	17.85	21.57	21.86	79.81	212.75

682 4.2.2 Best AI Model Finetuned by AEIO Algorithm

683 This section will focus on fine-tuning the hyperparameters of the numerical model to enhance its
684 performance in predicting deep-seated **landslides displacement**. The AEIO algorithm will fine-tune the
685 hyperparameters of the study's best numerical AI model, the R-GRU model. Details regarding the names
686 and search ranges of the hyperparameters are outlined in Table 8. The objective function of the AEIO
687 algorithm during the fine-tuning process is to minimize the MAPE value of the R-GRU model.

688 Table 9 illustrates the results of the fine-tuning process. From this table, it is observed that the AEIO
689 algorithm has successfully identified the optimal hyperparameters of the R-GRU model, significantly
690 improving the prediction accuracy of this model. For instance, the MAPE in predicting 1-day-ahead
691 displacement of R-GRU before fine-tuning was 7.9%, but this number decreased to only 3.03% after fine-
692 tuning. **All other predictions similarly show a decreasing trend.**

693 Fine-tuning the R-GRU model using AEIO will maximize its potential, minimizing the prediction
694 error to the lowest possible level. Therefore, the results obtained in this section reflect the actual quality
695 of the dataset as well as the level of difficulty in prediction. Specifically, based on the results in Table 9,
696 it is observed that the predictions for one-day ahead displacement (with MAPE of 3.03% and 3.94%)
697 consistently outperform those for seven-days ahead displacement (with MAPE of 6.38% and 7.96%).

698 One-day-ahead predictions have a shorter time horizon, making them less affected by environmental
699 fluctuations and making changes more accessible to predict. Conversely, in the case of seven-day-ahead
700 displacement prediction, this timeframe is long enough for various factors, such as weather conditions and
701 human interventions, to occur, increasing uncertainty and volatility in the predicted figures.

702 Additionally, Table 9 indicates that predictions from the dataset of the E-2 station consistently
 703 outperform those of the SAA station. **Specifically, the displacement prediction at the E-2 station is 3.03%**
 704 **and 6.38%, better than the corresponding numbers for the SAA station, which are 3.94% and 7.96%,**
 705 **respectively. This is attributed to the dataset collected by the E-2 station being more comprehensive and**
 706 **gathered over a more extended period than the SAA station (as shown in Table 4).**

707 Table 10 presents the optimal hyperparameters identified by the AEIO algorithm. Furthermore, in
 708 terms of running time, most models, after fine-tuning, exhibit longer running times compared to the
 709 original model. However, this increase is entirely acceptable since the additional running time is minimal,
 710 and the benefits of fine-tuning are significant, as mentioned above, aiding in the ~~model's~~ model's more
 711 efficient operation.

712 Table 8. Search ranges of the hyperparameters of the optimal hybrid numerical models (Chou and Nguyen,
 713 2023).

Hybrid model	Hyperparameter	Search range
AEIO-R-GRU	Window size	[1-720]
	Number of hidden units	[1-400]
	Learning rate	[0.0001, 0.5]
	Dropout	[0.00, 0.99]
	Number of epochs	[10, 120]
	Batch size	[32, 64]

714 Table 9. Performance results of hybrid time-series deep learning model with AEIO in deep-seated
 715 landslide prediction

	Model	MAPE (%)	MAE (mm)	RMSE (mm)	Time (s)
One-day- ahead displacement prediction	E-2-station				
	AEIO-R-GRU	3.03	6.89	17.98	196
	SAA-station				
	AEIO-R-GRU	3.94	4.16	11.20	184
Seven-day- ahead of displacement prediction	E-2-station				
	AEIO-R-GRU	6.38	10.02	18.05	261
	SAA-station				
	AEIO-R-GRU	7.96	12.49	7.82	248

716
 717 Table 10. Optimal hyperparameter of time series deep learning model found by AEIO algorithm

	Model	Window size	Number of hidden units	Dropout rate	Learning rate	Number of epochs	Batch size
One-day-ahead displacement prediction	E-2-station						
	AEIO-R-GRU	41	81	0.27	0.7	18	64
	SAA- station						
	AEIO-R-GRU	54	145	0.19	0.46	32	32
Seven-day-ahead of displacement prediction	E-2- station						
	AEIO-R-GRU	97	164	0.24	0.61	20	32
	SAA- station						
	AEIO-R-GRU	69	147	0.28	0.31	17	32

718 4.2.3 CNN Models

719 This section presents the results of utilizing CNN models, including VGG, ResNet, Inception,
720 Xception, DenseNet, and NASNet, to predict deep-seated landslide displacement. The CNN models in
721 this part use the default settings (Chou and Nguyen, 2023). Table 11 displays the prediction error results
722 of the CNN models for one-day-ahead and seven-day-ahead forecasts for both E-2 and SAA stations.

723 The prediction results demonstrate that most CNN models produce highly accurate predictions.
724 Specifically, predictions made by VGG, ResNet, MobileNet, DenseNet, and Inception exhibit MAPE
725 values below 5%. Among these, MobileNet and DenseNet201 emerge as the two models with the highest
726 accuracy. For one-day-ahead prediction, the best model for predicting displacement at the E-2 station is
727 MobileNet, with a MAPE of 4.11%, and the best model for predicting displacement at the SAA station is
728 DenseNet201, with a MAPE of 6.36%. For seven-day-ahead prediction, the best model for predicting
729 displacement at the E-2 station is DenseNet201, with a MAPE of 5.3%, and the best model for predicting
730 displacement at the SAA station is MobileNet, with a MAPE of 6.8%. These models will be selected
731 accordingly for fine-tuning in the subsequent section.

732 Regarding running time, the CNN models in this section exhibit significantly longer running times
733 compared to the numerical models in the previous sections. For example, the running time of the best
734 CNN model to predict one-day-ahead displacement at the E-2 station—MobileNet—is 1.21 hours. In
735 contrast, the running time of the best single numerical model for predicting this index is 159.97 seconds.

736 While CNN models yield better prediction results, considering their extended running times, users
737 need to weigh practical considerations before opting for this type of model. For instance, CNN models
738 should be employed in cases requiring accurate predictions for research and measurement purposes.
739 Conversely, numerical models like R-GRU are more suitable for real-time predictions and computations
740 on low-performance devices.

741 Table 11. Performance results of the CNN models for deep-seated displacement prediction

Model	MAPE (%)		MAE (mm)		RMSE (mm)		Time (hour)	
	1-day-ahead	7-day-ahead	1-day-ahead	7-day-ahead	1-day-ahead	7-day-ahead	1-day-ahead	7-day-ahead
E-2- station								
VGG16	4.58	7.38	12.73	13.97	26.54	35.69	3.03	3.31
VGG19	4.47	6.30	12.53	15.11	25.74	32.82	3.14	2.82
ResNet50V2	4.87	7.68	15.28	12.52	31.82	27.19	2.99	3.44
ResNet101V2	4.61	6.60	9.81	9.08	34.67	32.74	2.24	2.96
ResNet152V2	4.71	6.46	7.26	12.60	21.13	19.08	2.94	2.05
InceptionV3	4.99	7.30	11.18	11.65	32.97	34.92	2.43	3.27
InceptionRestNetV2	13.32	15.78	22.51	27.08	76.75	61.11	3.22	3.08
Xception	5.27	7.34	11.60	10.20	35.86	30.68	2.94	3.29
MobileNet	4.11	8.92	12.22	13.62	47.43	31.72	1.21	1.44
DenseNet121	11.15	11.13	16.30	21.49	37.68	46.51	3.32	3.99
DenseNet169	4.74	7.86	11.44	12.20	17.09	36.28	3.02	3.52
DenseNet201	4.66	5.30	8.11	7.44	21.82	10.39	2.09	2.29
NASNetMobile	13.82	15.91	31.00	19.52	46.07	55.65	2.53	3.13
NASNetLarge	13.20	34.23	20.46	61.81	61.52	75.39	3.89	3.93
SAA- station								
VGG16	5.76	7.90	6.07	12.76	9.48	8.95	3.14	3.36
VGG19	5.95	7.32	9.14	13.45	11.68	7.03	3.55	3.20
ResNet50V2	9.87	9.35	12.43	13.81	15.71	9.75	4.57	3.83
ResNet101V2	8.48	17.68	10.56	19.36	11.47	21.94	3.54	3.40
ResNet152V2	9.43	11.42	12.32	10.35	14.91	13.27	3.35	3.88
InceptionV3	10.96	8.11	12.73	9.13	14.48	12.71	3.80	3.18
InceptionRestNetV2	9.86	11.08	13.51	16.75	18.04	21.59	3.23	2.91
Xception	7.42	7.28	7.82	7.08	10.13	10.47	3.48	3.60
MobileNet	7.12	6.80	8.28	9.92	11.58	13.83	1.43	2.13
DenseNet121	8.69	11.69	8.56	14.39	12.54	15.76	3.93	3.42
DenseNet169	6.55	9.56	6.16	9.61	11.08	15.51	3.60	3.76
DenseNet201	6.36	10.45	7.46	11.62	9.37	14.51	2.51	3.13
NASNetMobile	10.31	22.12	13.86	62.04	18.95	43.51	3.56	2.88

Model	MAPE (%)		MAE (mm)		RMSE (mm)		Time (hour)	
	1-day-ahead	7-day-ahead	1-day-ahead	7-day-ahead	1-day-ahead	7-day-ahead	1-day-ahead	7-day-ahead
NASNetLarge	10.25	13.69	11.20	14.05	15.95	19.09	3.18	3.34

742 4.2.4 Best CNN Models Finetuned by AEIO Algorithm

743 In this section, as analyzed in part 4.2.3, the AEIO algorithm will sequentially fine-tune CNN models
744 to enhance prediction accuracy. Table 12 illustrates the search range of hyperparameters for the CNN
745 models to be fine-tuned. Table 13 presents the performance results of the CNN models after being fine-
746 tuned.

747 However, a challenge in this section is that CNN models primarily analyze and learn from image
748 data. Therefore, numerical data must be converted into image data before training. This poses a challenge
749 because current computer hardware may need to be fully capable of efficiently converting numerical data
750 into images for each computation. Hence, this study utilizes the optimal window sizes previously
751 identified for fine-tuning numerical models (Table 10) for this scenario and employs these fixed window
752 sizes for CNN models.

753 The results of the fine-tuning process demonstrate that the AEIO has successfully identified the
754 optimal hyperparameters for the CNN models, enhancing their accuracy. For instance, in the case of the
755 MobileNet model used for one-day-ahead prediction at the E-2 station, the fine-tuning process reduced
756 the MAPE of this model from 4.11% to 2.81%. A similar trend is also observed in the remaining prediction
757 scenarios.

758 Furthermore, similar to the case of AEIO-R-GRU, the CNN models exhibit the same trend, where
759 one-day-ahead predictions are more accurate than seven-day-ahead predictions. Similarly, forecasts at the
760 E-2 station demonstrate higher accuracy than predictions at the SAA station. The rationale for this has
761 been explained in section 4.2.2. Lastly, the optimal hyperparameters of each CNN model, identified by
762 the AEIO algorithm, are presented in Table 14. ~~Compared to models in previous sections,~~ CNN models
763 with optimal hyperparameters ~~obtained in this section exhibit the most minor errors, indicating that these~~
764 are the most effective models in this study for predicting ~~deep-seated displacement landslide occurrences.~~
765 Table 12. Search ranges of the hyperparameters of the optimal hybrid numerical models (Chou and
766 Nguyen, 2023).

Hybrid model	Hyperparameter	Search range
AEIO-CNN	Learning rate	[0.00, 0.1]
	Decay	[0.00, 0.1]

Hybrid model	Hyperparameter	Search range
	Momentum	[0.00, 0.99]
	Epsilon	[1.0e-7, 0.001]
	Dropout	[0.00, 0.99]
	Epochs	[10, 120]
	Batch size	[32, 64]

767 Table 13. Performance results of best CNN models with AEIO in deep-seated landslide prediction

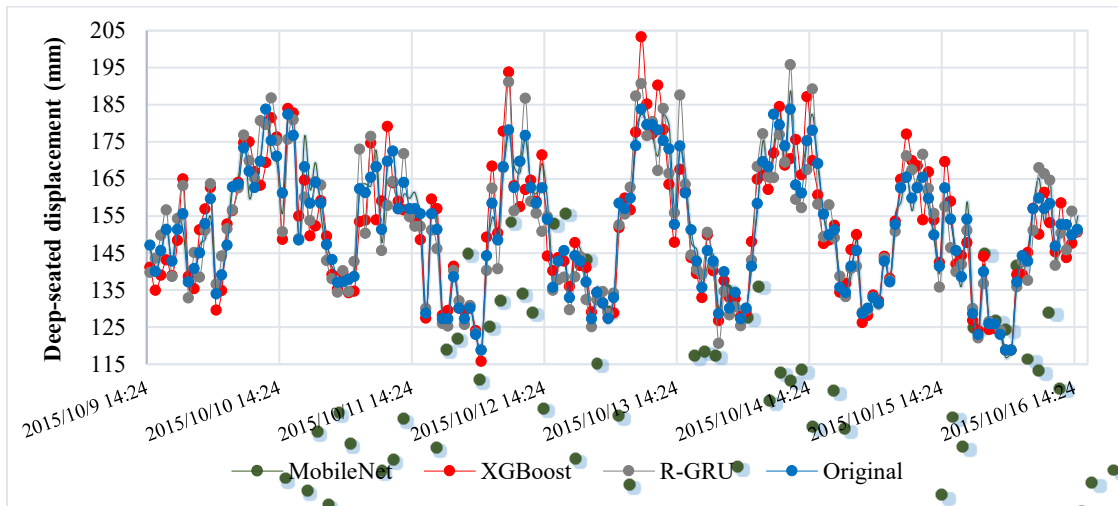
	Model	MAPE (%)	MAE (mm)	RMSE (mm)	Time (hour)
One-day-ahead displacement prediction	E-2-station				
	AEIO-MobileNet	2.81	5.09	11.92	1.25
	SAA-station				
	AEIO-DenseNet201	3.30	6.32	15.65	3.48
Seven-day-ahead of displacement prediction	E-2-station				
	AEIO-DenseNet201	4.30	5.32	15.65	3.48
	SAA-station				
	AEIO-MobileNet	5.63	9.35	14.27	3.39

768

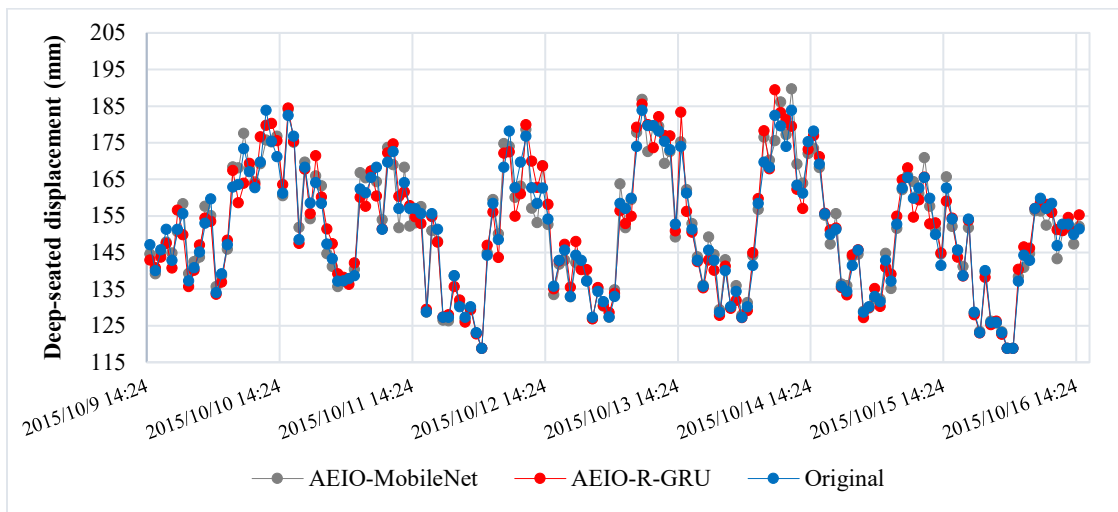
769 Table 14. Optimal hyperparameter of CNN models found by AEIO algorithm

	Model	Learning rate	Decay	Momentum	Epsilon	Dropout	Epochs	Batch size
One-day-ahead displacement prediction	E-2-station							
	AEIO-MobileNet	0.0011	0.00095	0.00001	3.0e-7	0.56	15	64
	SAA-station							
	AEIO-DenseNet201	0.00012	0.0012	0.00011	1.0e-7	0.49	16	64
Seven-day-ahead of displacement prediction	E-2-station							
	AEIO-DenseNet201	0.0012	0.0011	0.00022	1.0e-7	0.51	15	64
	SAA-station							
	AEIO-MobileNet	0.00014	0.00098	0.00011	2.0e-7	0.50	14	64

770 Figure 10 illustrates the differences between typical AI models' actual and predicted deep-seated
 771 displacement. Specifically, Figure 10a compares the performance of single models against the predicted
 772 values, while Figure 10b does the same for hybrid models. The chart shows hybrid models demonstrate
 773 superior predictive capability for deep-seated landslides compared to single models. This is evident from
 774 the displacement line of the hybrid models in Figure 10b, which closely aligns with the actual deep-seated
 775 displacement and significantly outperforms the single models depicted in Figure 10a.



776 a) Prediction results of deep-seated displacement by single AI models.



778 b) Prediction results of deep-seated displacement by AI models optimized using the AEIO algorithm.

779 Figure 10. Graph comparing the real and predicted deep-seated displacement.

780 **4.3 Discussion**

781 This study centers on landslides in Lushan Mountain, Taiwan, adopting a fundamentally different
 782 approach than previous research. While past studies primarily focused on constructing AI models for
 783 classification, calculating the probability of landslide occurrences, and generating landslide susceptibility
 784 maps (Balogun et al., 2021; Hakim et al., 2022; Jaafari et al., 2022), our study is oriented towards
 785 predicting displacement to provide warnings about potential landslide hazards.
 786

787 As utilized in our calculations, computing deep-seated displacement offers several benefits. Firstly,
788 understanding internal displacements provides accurate information for engineers to assess the resilience
789 of structures and infrastructure in at-risk areas, facilitating the issuance of sensible warnings. Secondly,
790 forecasting deep-seated displacement offers insights into the severity of the disaster, aiding in effective
791 evacuation and rescue planning.

792 Moreover, unlike AI models in previous studies (Balogun et al., 2021; Hakim et al., 2022; Jaafari et
793 al., 2022), our research incorporates machine learning, time series deep learning, and CNN models,
794 utilizing metaheuristic optimization algorithms to fine-tune their hyperparameters. However, the novelty
795 of our study lies in adopting pre-trained models, such as MobileNet, DenseNet, Inception, and VGG,
796 rather than ~~conventional standard CNN models. The practicality of employing these pre-trained models~~
797 ~~has demonstrated effectiveness in predicting displacement in this research.~~

798 By employing various AI models, this study identifies the most effective model for predicting deep-
799 seated landslides and offers a comprehensive overview of the performance of different AI models. Initially,
800 machine learning models exhibited relatively high prediction errors, with MAPE ranging from 8.14% to
801 15.19%. This performance was generally lower than time-series deep learning models, which showed
802 MAPEs ranging from 7.9% to 14.73%. The superior performance of the time series deep learning models
803 is attributed to their ability to process sequential data and retain information from previous steps. This
804 enables them to learn patterns from the dataset more effectively than traditional machine learning models.

805 However, compared to CNN models, the results of the time series deep learning models are not as
806 strong. This disparity is attributed to CNN's superior learning mechanism. The convolutional and pooling
807 layers in CNN enable robust feature extraction from the input data. Convolutional layers are particularly
808 effective at identifying complex patterns and subtle features within time series data, primarily when spatial
809 correlations exist. This capability allows CNN to uncover essential features that other models might
810 overlook.

811 The models developed in this study demonstrate predictive solid capabilities for deep-seated
812 displacement. Among them, the AEIO-MobileNet model is the most effective, achieving predictions with
813 deficient error, indicated by a MAPE of 2.81%. However, these models' practical applicability in real-
814 world scenarios must be improved due to the time-consuming processes involved in data collection,
815 processing, and AI model operation, making timely predictions challenging. Meanwhile, there have been
816 studies that successfully built real-time landslide detection systems (Wang et al., 2023; Das et al., 2020;
817 C. et al., 2021). We acknowledge this limitation of our study. Therefore, future research endeavors will
818 aim to address this issue.

819 The input data used for the AI models were selected because they significantly influence the
820 likelihood of deep-seated landslides, as detailed in Section 3.6. However, a limitation of this study is that

821 it does not evaluate the relative importance of each input data type on prediction accuracy. Future research
822 should explore the impact of different combinations of input data on AI model performance. This could
823 help identify the significance of each input type and potentially reveal the optimal combination of inputs
824 to enhance prediction accuracy further.

825 **5. Conclusion and Recommendations**

826 This study addresses the persistent threat of landslides, a primary concern due to their severe impact
827 on lives and property. Employing various AI models, such as machine learning, time series deep learning,
828 CNN models, and metaheuristic optimization algorithms, the research focuses on predicting deep-seated
829 landslides at Lushan Mountain in Ren'ai Township, Nantou County. The study aims to enhance early
830 prediction accuracy by utilizing eight years of displacement and groundwater level data from Lushan
831 Mountain and weather data from the POWER project. The predictions cover one-day and seven-day
832 intervals, serving diverse purposes in landslide forecasting for timely evacuation. The research explores
833 single and hybrid AI models to determine the most effective approach. The following conclusions are
834 drawn from this research:

835 (a). CNN models optimized by the novel AEIO algorithm yield the best prediction results. In particular,
836 AEIO-MobileNet predicts one-day-ahead displacement at the E-2 station with a MAPE score of only
837 2.81%, demonstrating high accuracy.

838 (b). While CNN models boast high prediction accuracy, their computational time is also considerable.
839 Therefore, decisions regarding their usage should also consider real-world constraints.

840 (c). The AEIO-R-GRU model also yields reasonably good prediction results, although not on par with
841 CNN models. The best result achieved by the AEIO-R-GRU model is a MAPE of 3.03% for one-day-
842 ahead prediction at the E-2 station.

843 (d). The AEIO algorithm has successfully fine-tuned hyperparameters for AI models. Especially in the
844 case of predicting one-day-ahead displacement, it has aided the MobileNet model in improving its
845 predictive capability by 31.6%, enabling this model to provide more accurate predictions.

846 (e). The prediction results from the E-2 station consistently outperform those from the SAA station. This
847 is attributed to the fact that data from the E-2 station has been collected over a longer and more
848 comprehensive period.

849 (f). The study results demonstrate that AI models can accurately predict deep-seated displacement, which
850 can be implemented in real-world scenarios.

851 **Declare of Competing Interest**

852 The authors declare that there are no known conflicts of interest associated with this publication, and
853 there has been no significant financial support for this work that could have influenced its outcome.

854 **Data Availability Statement**

855 The data and source codes supporting this study's findings are available at
856 <https://www.researchgate.net/profile/Jui-Sheng-Chou> and from the corresponding author upon reasonable
857 request.

858 **Acknowledgments**

859 The authors thank the National Science and Technology Council (NSTC), Taiwan, for financially
860 supporting this research under NSTC grants 112-2221-E-011-033-MY3 and 111-2221-E-011-037-MY3.

861 **Author contribution**

862 Jui-Sheng Chou: conceptualization, methodology, supervision, writing manuscript, reviewing, and
863 editing. Hoang-Minh Nguyen: data processing, coding, and writing manuscript. Huy-Phuong Phan: Data
864 processing, coding, and manuscript writing. Kuo-Lung Wang: data preparation, supervision, and
865 reviewing.

866 **References**

- 867 Aggarwal, A., Alshehri, M., Kumar, M., Alfarraj, O., Sharma, P., and Pardasani, K. R.: Landslide
868 data analysis using various time-series forecasting models, *Comput Electr Eng*, 88,
869 <https://doi.org/10.1016/j.compeleceng.2020.106858>, 2020.
- 870 Alzubaidi, L., Zhang, J., Humaidi, A. J., Al-Dujaili, A., Duan, Y., Al-Shamma, O., Santamaría,
871 J., Fadhel, M. A., Al-Amidie, M., and Farhan, L.: Review of deep learning: concepts, CNN
872 architectures, challenges, applications, future directions, *Journal of Big Data*, 8, 53,
873 <https://doi.org/10.1186/s40537-021-00444-8>, 2021.
- 874 Balogun, A. L., Rezaie, F., Pham, Q. B., Gigovic, L., Drobnyak, S., Aina, Y. A., Panahi, M.,
875 Yekeen, S. T., and Lee, S.: Spatial prediction of landslide susceptibility in western Serbia using
876 hybrid support vector regression (SVR) with GWO, BAT and COA algorithms, *Geosci Front*, 12,
877 <https://doi.org/10.1016/j.gsf.2020.10.009>, 2021.
- 878 Breiman, L.: *Classification and Regression Trees*, Taylor & Francis Group, New York,
879 <https://doi.org/10.1201/9781315139470>, 1984.
- 880 C., P., R., A., Kanwar, V. S., and B., N.: Design and Development of Real-time landslide early
881 warning system through low cost soil and rainfall sensors, *Materials Today: Proceedings*, 45,
882 5649-5654, <https://doi.org/10.1016/j.matpr.2021.02.456>, 2021.
- 883 Caleca, F., Scaini, C., Frodella, W., and Tofani, V.: Regional-scale landslide risk assessment in
884 Central Asia, *Nat Hazard Earth Sys*, 24, 13-27, <https://doi.org/10.5194/nhess-24-13-2024>, 2024.
- 885 Chae, B.-G., Park, H. J., Catani, F., Simoni, A., and Berti, M.: Landslide prediction, monitoring
886 and early warning: a concise review of state-of-the-art, *Geosciences Journal*, 21, 1033-1070,
887 <https://doi.org/10.1007/s12303-017-0034-4>, 2017.
- 888 Chen; T. and Guestrin, C.: XGBoost: A Scalable Tree Boosting System, In *Proceedings of the*
889 *22nd ACM SIGKDD International Conference on Knowledge Discovery and Data Mining*, New
890 York, NY, USA, 785–794, <https://doi.org/10.1145/2939672.2939785>, 2016.
- 891 Chigira, M.: September 2005 rain-induced catastrophic rockslides on slopes affected by deep-
892 seated gravitational deformations, Kyushu, southern Japan, *Eng Geol*, 108, 1-15,
893 <https://doi.org/10.1016/j.enggeo.2009.03.005>, 2009.

894 Chollet, F.: Xception: Deep Learning with Depthwise Separable Convolutions, 2017 IEEE
895 Conference on Computer Vision and Pattern Recognition (CVPR), Honolulu, HI, USA, July 21,
896 2017, <https://doi.org/10.48550/arXiv.1610.02357>, 2017.

897 Chou, J. S. and Ngo, N. T.: Time series analytics using sliding window metaheuristic
898 optimization-based machine learning system for identifying building energy consumption patterns,
899 Appl Energ, 177, 751-770, <https://doi.org/10.1016/j.apenergy.2016.05.074>, 2016.

900 Chou, J. S. and Nguyen, N. Q.: Forecasting Regional Energy Consumption via Jellyfish Search-
901 Optimized Convolutional-Based Deep Learning, Int J Energ Res, Volume 2023,
902 <https://doi.org/10.1155/2023/3056688>, 2023.

903 Corominas, J., van Westen, C., Frattini, P., Cascini, L., Malet, J. P., Fotopoulou, S., Catani, F.,
904 Van Den Eeckhaut, M., Mavrouli, O., Agliardi, F., Pitilakis, K., Winter, M. G., Pastor, M., Ferlisi,
905 S., Tofani, V., Hervás, J., and Smith, J. T.: Recommendations for the quantitative analysis of
906 landslide risk, Bulletin of Engineering Geology and the Environment, 73, 209-263,
907 <https://doi.org/10.1007/s10064-013-0538-8>, 2014.

908 Cotecchia, F., Santaloia, F., and Tagarelli, V.: Towards A Geo-Hydro-Mechanical
909 Characterization of Landslide Classes: Preliminary Results, Applied Sciences, 10,
910 <https://doi.org/10.3390/app10227960>, 2020.

911 Crosta, G. B. and Agliardi, F.: Failure forecast for large rock slides by surface displacement
912 measurements, Canadian Geotechnical Journal, 40, 176-191, <https://doi.org/10.1139/t02-085>,
913 2003.

914 Dahal, A., Tanyas, H., Westen, C. v., Meijde, M. v. d., Mai, P. M., Huser, R., and Lombardo, L.:
915 Space–time landslide hazard modeling via Ensemble Neural Networks, Nat Hazard Earth Sys, 24,
916 823-845, <https://doi.org/10.5194/nhess-24-823-2024>, 2024.

917 Das, K., Majumdar, S., Moulik, S., and Fujita, M.: Real-Time Threshold-based Landslide
918 Prediction System for Hilly Region using Wireless Sensor Networks, 2020 IEEE International
919 Conference on Consumer Electronics - Taiwan (ICCE-Taiwan), Taoyuan, Taiwan,
920 <https://doi.org/10.1109/ICCE-Taiwan49838.2020.9258181>, 2020.

921 Das, S., Sarkar, S., and Kanungo, D. P.: Rainfall-induced landslide (RFIL) disaster in Dima Hasao,
922 Assam, Northeast India, Landslides, 19, 2801-2808, [https://doi.org/10.1007/s10346-022-01962-](https://doi.org/10.1007/s10346-022-01962-z)
923 [z](https://doi.org/10.1007/s10346-022-01962-z), 2022.

924 Di Nunno, F., de Marinis, G., and Granata, F.: Short-term forecasts of streamflow in the UK based
925 on a novel hybrid artificial intelligence algorithm, Scientific Reports, 13, 7036,
926 <https://doi.org/10.1038/s41598-023-34316-3>, 2023.

927 Drucker, H., Burges, C. J. C., Kaufman, L., Smola, A., and Vapnik, V.: Support vector regression
928 machines, NIPS'96: Proceedings of the 9th International Conference on Neural Information
929 Processing Systems, 155-161, 1996.

930 Elman, J. L.: Finding Structure in Time, Cognitive Sci, 14, 179-211, [https://doi.org/10.1016/0364-](https://doi.org/10.1016/0364-0213(90)90002-E)
931 [0213\(90\)90002-E](https://doi.org/10.1016/0364-0213(90)90002-E), 1990.

932 Fu, W. X. and Liao, Y.: Non-linear shear strength reduction technique in slope stability calculation,
933 Comput Geotech, 37, 288-298, <https://doi.org/10.1016/j.compgeo.2009.11.002>, 2010.

934 Geertsema, M., Hungr, O., Schwab, J. W., and Evans, S. G.: A large rockslide-debris avalanche
935 in cohesive soil at Pink Mountain, northeastern British Columbia, Canada, *Eng Geol*, 83, 64-75,
936 <https://doi.org/10.1016/j.enggeo.2005.06.025>, 2006.

937 Hakim, W. L., Rezaie, F., Nur, A. S., Panahi, M., Khosravi, K., Lee, C. W., and Lee, S.:
938 Convolutional neural network (CNN) with metaheuristic optimization algorithms for landslide
939 susceptibility mapping in Icheon, South Korea, *J Environ Manage*, 305,
940 <https://doi.org/10.1016/j.jenvman.2021.114367>, 2022.

941 Han, H. G., Chen, Q. L., and Qiao, J. F.: Research on an online self-organizing radial basis
942 function neural network, *Neural Comput Appl*, 19, 667-676, <https://doi.org/10.1007/s00521-009-0323-6>, 2010.

944 Han, J., Kamber, M., and Pei, J.: *Data Mining: Concepts and Techniques*, Southeast Asia Edition,
945 Morgan Kaufmann Publishers Inc., San Francisco, CA, United States, 696 pp.,
946 <https://doi.org/10.1016/C2009-0-61819-5>, 2006.

947 He, K., Zhang, X., Ren, S., and Sun, J.: Deep Residual Learning for Image Recognition, 2016
948 IEEE Conference on Computer Vision and Pattern Recognition,
949 <https://doi.org/10.48550/arXiv.1512.03385>, 2016.

950 He, R., Zhang, W., Dou, J., Jiang, N., Xiao, H., and Zhou, J.: Application of artificial intelligence
951 in three aspects of landslide risk assessment: A comprehensive review, *Rock Mechanics Bulletin*,
952 <https://doi.org/https://doi.org/10.1016/j.rockmb.2024.100144>, 2024.

953 Howard, A. G., Zhu, M., Chen, B., Kalenichenko, D., Wang, W., Weyand, T., Andreetto, M., and
954 Adam, H.: MobileNets: Efficient Convolutional Neural Networks for Mobile Vision Applications,
955 *CoRR*, abs/1704.04861, <https://doi.org/10.48550/arXiv.1704.04861>, 2017.

956 Hu, B., Su, G., Jiang, J., Sheng, J., and Li, J.: Uncertain Prediction for Slope Displacement Time-
957 Series Using Gaussian Process Machine Learning, *Ieee Access*, PP, 1-1,
958 <https://doi.org/10.1109/ACCESS.2019.2894807>, 2019.

959 Hu, X. L., Wu, S. S., Zhang, G. C., Zheng, W. B., Liu, C., He, C. C., Liu, Z. X., Guo, X. Y., and
960 Zhang, H.: Landslide displacement prediction using kinematics-based random forests method: A
961 case study in Jinping Reservoir Area, China, *Eng Geol*, 283,
962 <https://doi.org/10.1016/j.enggeo.2020.105975>, 2021.

963 Huang, G., Liu, Z., Maaten, L. v. d., and Weinberger, K. Q.: Densely Connected Convolutional
964 Networks, 2017 IEEE Conference on Computer Vision and Pattern Recognition (CVPR),
965 <https://doi.org/10.1109/CVPR.2017.243>, 2017.

966 Huang, R. Q. and Fan, X. M.: The landslide story, *Nat Geosci*, 6, 325-326,
967 <https://doi.org/10.1038/ngeo1806>, 2013.

968 Hungr, O., Leroueil, S., and Picarelli, L.: The Varnes classification of landslide types, an update,
969 *Landslides*, 11, 167-194, <https://doi.org/10.1007/s10346-013-0436-y>, 2014.

970 Jaafari, A., Jaafari, A., Panahi, M., Panahi, M., Mafi-Gholami, D., Mafi-Gholami, D., Rahmati,
971 O., Rahmati, O., Shahabi, H., Shahabi, H., Shirzadi, A., Shirzadi, A., Lee, S., Lee, S., Bui, D. T.,
972 Bui, D. T., Pradhan, B., and Pradhan, B.: Swarm intelligence optimization of the group method
973 of data handling using the cuckoo search and whale optimization algorithms to model and predict
974 landslides, *Appl Soft Comput*, 116, <https://doi.org/10.1016/j.asoc.2021.108254>, 2022.

975 Jiang, J., Ehret, D., Xiang, W., Rohn, J., Huang, L., Yan, S., and Bi, R.: Numerical simulation of
976 Qiaotou Landslide deformation caused by drawdown of the Three Gorges Reservoir, China,
977 *Environmental Earth Sciences*, 62, 411-419, <https://doi.org/10.1007/s12665-010-0536-0>, 2011.

978 Jones, J. N., Bennett, G. L., Abanco, C., Matera, M. A. M., and Tan, F. J.: Multi-event assessment
979 of typhoon-triggered landslide susceptibility in the Philippines, *Nat Hazard Earth Sys*, 23, 1095-
980 1115, <https://doi.org/10.5194/nhess-23-1095-2023>, 2023.

981 Keqiang, H., Zhiliang, W., Xiaoyun, M., and Zengtao, L.: Research on the displacement response
982 ratio of groundwater dynamic augment and its application in evaluation of the slope stability,
983 *Environmental Earth Sciences*, 74, 5773-5791, <https://doi.org/10.1007/s12665-015-4595-0>, 2015.

984 Kilburn, C. R. J. and Petley, D. N.: Forecasting giant, catastrophic slope collapse: lessons from
985 Vajont, Northern Italy, *Geomorphology*, 54, 21-32, [https://doi.org/10.1016/S0169-555x\(03\)00052-7](https://doi.org/10.1016/S0169-555x(03)00052-7), 2003.

987 Kumar, D., lakhwan, N., and Rawat, A.: Study and Prediction of Landslide in Uttarkashi,
988 Uttarakhand, India Using GIS and ANN, *American Journal of Neural Networks and Applications*
989 3, <https://doi.org/10.11648/j.ajjna.20170306.12>, 2017.

990 Lau, Y. M., Wang, K. L., Wang, Y. H., Yiu, W. H., Ooi, G. H., Tan, P. S., Wu, J., Leung, M. L.,
991 Lui, H. L., and Chen, C. W.: Monitoring of rainfall-induced landslides at Songmao and Lushan,
992 Taiwan, using IoT and big data-based monitoring system, *Landslides*, 20, 271-296,
993 <https://doi.org/10.1007/s10346-022-01964-x>, 2023.

994 Lee, Y. F. and Chi, Y. Y.: Rainfall-induced landslide risk at Lushan, Taiwan, *Eng Geol*, 123, 113-
995 121, <https://doi.org/10.1016/j.enggeo.2011.03.006>, 2011.

996 Li, H., Xu, Q., He, Y., and Deng, J.: Prediction of landslide displacement with an ensemble-based
997 extreme learning machine and copula models, *Landslides*, 15, 2047-2059,
998 <https://doi.org/10.1007/s10346-018-1020-2>, 2018.

999 Lin, C. W., Tseng, C. M., Tseng, Y. H., Fei, L. Y., Hsieh, Y. C., and Tarolli, P.: Recognition of
1000 large scale deep-seated landslides in forest areas of Taiwan using high resolution topography, *J*
1001 *Asian Earth Sci*, 62, 389-400, <https://doi.org/10.1016/j.jseaes.2012.10.022>, 2013.

1002 Lin, H. H., Lin, M. L., Lu, J. H., Chi, C. C., and Fei, L. Y.: Deep-seated gravitational slope
1003 deformation in Lushan, Taiwan: Transformation from cleavage-controlled to weakened rockmass-
1004 controlled deformation, *Eng Geol*, 264, <https://doi.org/10.1016/j.enggeo.2019.105387>, 2020.

1005 Liu, C. Y., Jiang, Z. S., Han, X. S., and Zhou, W. X.: Slope displacement prediction using
1006 sequential intelligent computing algorithms, *Measurement*, 134, 634-648,
1007 <https://doi.org/10.1016/j.measurement.2018.10.094>, 2019.

1008 Loche, M. and Scaringi, G.: Temperature and shear-rate effects in two pure clays: Possible
1009 implications for clay landslides, *Results Eng*, 20, <https://doi.org/10.1016/j.rineng.2023.101647>,
1010 2023.

1011 Margarint, M. C., Grozavu, A., and Patriche, C. V.: Assessing the spatial variability of coefficients
1012 of landslide predictors in different regions of Romania using logistic regression, *Nat Hazard Earth*
1013 *Sys*, 13, 3339-3355, <https://doi.org/10.5194/nhess-13-3339-2013>, 2013.

1014 Matsushi, Y. and Matsukura, Y.: Rainfall thresholds for shallow landsliding derived from
1015 pressure-head monitoring: cases with permeable and impermeable bedrocks in Boso Peninsula,
1016 Japan, *Earth Surf Proc Land*, 32, 1308-1322, <https://doi.org/10.1002/esp.1491>, 2007.

- 1017 McCulloch, W. and Pitts, A.: A Logical Calculus of the Ideas Immanent in Nervous Activity
1018 (1943), *Ideas That Created the Future*, 79-88, <https://doi.org/10.1007/BF02478259>, 2021.
- 1019 Miao, H. B. and Wang, G. H.: Prediction of landslide velocity and displacement from groundwater
1020 level changes considering the shear rate-dependent friction of sliding zone soil, *Eng Geol*, 327,
1021 <https://doi.org/10.1016/j.enggeo.2023.107361>, 2023.
- 1022 Millán-Arancibia, C. and Lavado-Casimiro, W.: Rainfall thresholds estimation for shallow
1023 landslides in Peru from gridded daily data, *Nat Hazard Earth Sys*, 23, 1191-1206,
1024 <https://doi.org/10.5194/nhess-23-1191-2023>, 2023.
- 1025 Mufundirwa, A., Fujii, Y., and Kodama, J.: A new practical method for prediction of
1026 geomechanical failure-time, *Int J Rock Mech Min*, 47, 1079-1090,
1027 <https://doi.org/10.1016/j.ijrmms.2010.07.001>, 2010.
- 1028 Perkins, J. P., Oakley, N. S., Collins, B. D., Corbett, S. C., and Burgess, W. P.: Characterizing the
1029 scale of regional landslide triggering from storm hydrometeorology, *Nat Hazard Earth Sys*,
1030 <https://doi.org/10.5194/egusphere-2024-873>, 2024.
- 1031 Peternel, T., Janža, M., Šegina, E., Bezak, N., and Maček, M.: Recognition of Landslide
1032 Triggering Mechanisms and Dynamics Using GNSS, UAV Photogrammetry and In Situ
1033 Monitoring Data, *Remote Sensing*, 14, <https://doi.org/10.3390/rs14143277>, 2022.
- 1034 Petley, D.: Global patterns of loss of life from landslides, *Geology*, 40, 927-930,
1035 <https://doi.org/10.1130/G33217.1>, 2012.
- 1036 Petley, D. N., Mantovani, F., Bulmer, M. H., and Zannoni, A.: The use of surface monitoring data
1037 for the interpretation of landslide movement patterns, *Geomorphology*, 66, 133-147,
1038 <https://doi.org/10.1016/j.geomorph.2004.09.011>, 2005.
- 1039 Pham, B. T., Pradhan, B., Bui, D. T., Prakash, I., and Dholakia, M. B.: A comparative study of
1040 different machine learning methods for landslide susceptibility assessment: A case study of
1041 Uttarakhand area (India), *Environ Modell Softw*, 84, 240-250,
1042 <https://doi.org/10.1016/j.envsoft.2016.07.005>, 2016.
- 1043 Pinyol, N. M., Alvarado, M., Alonso, E. E., and Zabala, F.: Thermal effects in landslide mobility,
1044 *Geotechnique*, 68, 528-545, <https://doi.org/10.1680/jgeot.17.P.054>, 2018.
- 1045 Preisig, G.: Forecasting the long-term activity of deep-seated landslides via groundwater flow and
1046 slope stability modelling, *Landslides*, 17, 1693-1702, [https://doi.org/10.1007/s10346-020-01427-](https://doi.org/10.1007/s10346-020-01427-1)
1047 [1](https://doi.org/10.1007/s10346-020-01427-1), 2020.
- 1048 Ruitang, L., Zhaowei, C., Zexiong, W., Zhenghan, Z., Jiahao, L., Zhencheng, G., and Yuchong,
1049 C.: *Mountain Slope Monitoring Guidelines (TGS-SLOPEM106)*, 2017.
- 1050 Shibasaki, T., Matsuura, S., and Hasegawa, Y.: Temperature-dependent residual shear strength
1051 characteristics of smectite-bearing landslide soils, *J Geophys Res-Sol Ea*, 122, 1449-1469,
1052 <https://doi.org/10.1002/2016jb013241>, 2017.
- 1053 Simonyan, K. and Zisserman, A.: Very Deep Convolutional Networks for Large-Scale Image
1054 Recognition, *ICLR2015*, <https://doi.org/10.48550/arXiv.1409.1556>, 2015.
- 1055 Srivastava, S., Anand, N., Sharma, S., Dhar, S., and Sinha, L. K.: *Monthly Rainfall Prediction*
1056 *Using Various Machine Learning Algorithms for Early Warning of Landslide Occurrence*, 2020

- 1057 International Conference for Emerging Technology (INCET), Belgaum, India, 5-7 June 2020, 1-
1058 7, <https://doi.org/10.1109/INCET49848.2020.9154184>, 2020.
- 1059 Stanton, J. M.: Galton, Pearson, and the Peas: A Brief History of Linear Regression for Statistics
1060 Instructors, Journal of Statistics Education, 9, <https://doi.org/10.1080/10691898.2001.11910537>,
1061 2001.
- 1062 Szegedy, C., Vanhoucke, V., Ioffe, S., Shlens, J., and Wojna, Z.: Rethinking the Inception
1063 Architecture for Computer Vision, 2016 IEEE Conference on Computer Vision and Pattern
1064 Recognition (CVPR), 2818-2826, <https://doi.org/https://doi.org/10.1109/CVPR.2016.308>, 2015.
- 1065 Take, W. A., Beddoe, R. A., Davoodi-Bilesavar, R., and Phillips, R.: Effect of antecedent
1066 groundwater conditions on the triggering of static liquefaction landslides, Landslides, 12, 469-
1067 479, <https://doi.org/10.1007/s10346-014-0496-7>, 2015.
- 1068 Thai Pham, B., Shirzadi, A., Shahabi, H., Omidvar, E., Singh, S. K., Sahana, M., Talebpour Asl,
1069 D., Bin Ahmad, B., Kim Quoc, N., and Lee, S.: Landslide Susceptibility Assessment by Novel
1070 Hybrid Machine Learning Algorithms, Sustainability-Basel, 11,
1071 <https://doi.org/10.3390/su11164386>, 2019.
- 1072 van Natijne, A. L., Bogaard, T. A., Zieher, T., Pfeiffer, J., and Lindenbergh, R. C.: Machine-
1073 learning-based nowcasting of the Vögelsberg deep-seated landslide: why predicting slow
1074 deformation is not so easy, Nat Hazard Earth Sys, 23, 3723-3745, [https://doi.org/10.5194/nhess-
1075 23-3723-2023](https://doi.org/10.5194/nhess-23-3723-2023), 2023.
- 1076 Wang, K.-L., Lin, M.-L., Lin, J.-T., Huang, S.-C., Liao, R.-T., and Chen, C.-W.: Monitoring of
1077 the Evolution of a Deep-Seated Landslide in Lushan Area, Taiwan, Engineering Geology for
1078 Society and Territory, 2, 1317-1320, [https://doi.org/https://doi.org/10.1007/978-3-319-09057-
1079 3_231](https://doi.org/https://doi.org/10.1007/978-3-319-09057-3_231), 2015.
- 1080 Wang, Y., Dong, J., Zhang, L., Deng, S. H., Zhang, G. K., Liao, M. S., and Gong, J. Y.: Automatic
1081 detection and update of landslide inventory before and after impoundments at the Lianghekou
1082 reservoir using Sentinel-1 InSAR, Int J Appl Earth Obs, 118,
1083 <https://doi.org/10.1016/j.jag.2023.103224>, 2023.
- 1084 Wu, J. H.: Seismic landslide simulations in discontinuous deformation analysis, Comput Geotech,
1085 37, 594-601, <https://doi.org/10.1016/j.compgeo.2010.03.007>, 2010.
- 1086 Xu, J., Jiang, Y., and Yang, C.: Landslide Displacement Prediction during the Sliding Process
1087 Using XGBoost, SVR and RNNs, Applied Sciences, 12, <https://doi.org/10.3390/app12126056>,
1088 2022.
- 1089 Xu, J., Li, H., Du, K., Yan, C., Zhao, X., Li, W., and Xu, X.: Field investigation of force and
1090 displacement within a strata slope using a real-time remote monitoring system, Environmental
1091 Earth Sciences, 77, 552, <https://doi.org/10.1007/s12665-018-7729-3>, 2018.
- 1092 Yang, B., Yin, K., Lacasse, S., and Liu, Z.: Time series analysis and long short-term memory
1093 neural network to predict landslide displacement, Landslides, 16, [https://doi.org/10.1007/s10346-
1094 018-01127-x](https://doi.org/10.1007/s10346-018-01127-x), 2019.
- 1095 Yang, S., Jin, A., Nie, W., Liu, C., and Li, Y.: Research on SSA-LSTM-Based Slope Monitoring
1096 and Early Warning Model, Sustainability-Basel, 14, <https://doi.org/10.3390/su141610246>, 2022.

- 1097 Zhang, L., Shi, B., Zhu, H., Yu, X. B., Han, H., and Fan, X.: PSO-SVM-based deep displacement
1098 prediction of Majiagou landslide considering the deformation hysteresis effect, *Landslides*, 18,
1099 179-193, <https://doi.org/10.1007/s10346-020-01426-2>, 2021.
- 1100 Zhang, W., Li, H., Tang, L., Gu, X., Wang, L., and Wang, L.: Displacement prediction of
1101 Jiuxianping landslide using gated recurrent unit (GRU) networks, *Acta Geotechnica*, 17, 1367-
1102 1382, <https://doi.org/10.1007/s11440-022-01495-8>, 2022.
- 1103 Zhang, W. G., Zhang, R. H., Wu, C. Z., Goh, A. T. C., Lacasse, S., Liu, Z. Q., and Liu, H. L.:
1104 State-of-the-art review of soft computing applications in underground excavations, *Geosci Front*,
1105 11, 1095-1106, <https://doi.org/10.1016/j.gsf.2019.12.003>, 2020.
- 1106 Zheng, H. Y., Liu, B., Han, S. Y., Fan, X. Y., Zou, T. Y., Zhou, Z. L., and Gong, H.: Research on
1107 landslide hazard spatial prediction models based on deep neural networks: a case study of
1108 northwest Sichuan, China, *Environmental Earth Sciences*, 81, [https://doi.org/10.1007/s12665-
1109 022-10369-x](https://doi.org/10.1007/s12665-022-10369-x), 2022.
- 1110 Zhou, C., Yin, K., Cao, Y., Ahmed, B., and Fu, X.: A novel method for landslide displacement
1111 prediction by integrating advanced computational intelligence algorithms, *Scientific Reports*, 8,
1112 7287, <https://doi.org/10.1038/s41598-018-25567-6>, 2018.
- 1113 Zoph, B., Vasudevan, V., Shlens, J., and Le, Q. V.: Learning Transferable Architectures for
1114 Scalable Image Recognition, 2018 IEEE/CVF Conference on Computer Vision and Pattern
1115 Recognition (CVPR), 8697-8710, <https://doi.org/10.1109/CVPR.2018.00907>, 2018.
- 1116